

Textural and chemical variations of magnetite from porphyry Cu-Au and Cu skarn deposits in the Zhongdian region, northwestern Yunnan, SW China

Jian-Heng Guo^{a,b}, Cheng-Biao Leng^{a,c,*}, Xing-Chun Zhang^a, Tehseen Zafar^{a,b}, Wei Terry Chen^a, Wei Zhang^a, Zhen-Dong Tian^{a,b}, Feng Tian^{a,b}, Chun-Kit Lai^d

^a State Key Laboratory of Ore Deposit Geochemistry, Institute of Geochemistry, Chinese Academy of Sciences, Guiyang 550081, PR China

^b University of Chinese Academy of Sciences, Beijing 100049, PR China

^c State Key Laboratory of Nuclear Resources and Environment, East China University of Technology, Nanchang 330013, PR China

^d Faculty of Science, Universiti Brunei Darussalam, Gadong BE1410, Brunei Darussalam, PR China

ARTICLE INFO

Keywords:

Porphyry system
Magnetite chemistry
LA-ICP-MS
SEM-EDS mapping
Dissolution-reprecipitation
Zhongdian region (SW China)

ABSTRACT

The Zhongdian region in northwestern Yunnan (SW China) hosts a number of important porphyry and skarn deposits. In this study, we integrate petrographic observations, SEM-EDS elemental mapping, EPMA and LA-ICP-MS geochemical analyses on magnetite from several key deposits in the region. Magnetite grains from the Pulang porphyry Cu-Au, Lannitang porphyry Au-Cu, Langdu Cu skarn, Disuga porphyry, and andesite of Tumugou Formation were analyzed to unravel the magnetite formation mechanism, and the relative oxygen fugacity of the porphyry/skarn ore-related hydrothermal fluids in this region.

Two types of magnetites (Magnetite I and II) have been identified. Magnetite I is commonly distributed in the chlorite and/or sericite alteration zone(s). Magnetite I grains are characterized by being textually inhomogeneous. The Magnetite I core (with local ilmenite exsolution lamellae) is Ti-Cr rich, indicative of a dominantly igneous origin. The Magnetite I core and its surrounding primary igneous minerals (biotite, amphibole and plagioclase) underwent late alteration. Magnetite I grains are characterized by core-rim texture, sharp core-rim contact, and irregular grain boundaries. These textural features indicate that Magnetite I may have undergone dissolution-reprecipitation processes, during which the Magnetite I core was chemically purified via losing Ti and gaining Fe. Magnetite II (in potassic and sericite alteration zones) is textually homogeneous with relatively low contents of Ti, Mg, Al, V, Ni, and Mn. We suggest that Magnetite II was formed by hydrothermal alteration. Compared to Magnetite II grains from the Pulang and Langdu deposits, those from the Lannitang deposit have lower Mn and V but higher Sn contents, indicative of higher oxygen fugacity of the hydrothermal fluids. We propose that binary plots such as Ti vs. Sc, V vs. Sn and Ga vs. Sn can distinguish the different origins of magnetites.

From an exploration perspective, Magnetite II from the altered Disuga porphyries has similar texture and composition to its counterpart from the potassically-altered Pulang porphyries. This, together with the presence of Cu-sulfide inclusions in the Disuga Magnetite I, suggests significant mineralization potential in these porphyries.

1. Introduction

Magnetite is a common accessory mineral in a wide range of igneous rocks, and a major metallic mineral in many types of ore deposits (Lindsley, 1976; Wechsler et al., 1984). Many cations (e.g., Al^{3+} , Ti^{4+} , Mg^{2+} , $\text{Mn}^{2+}/\text{Mn}^{4+}$, Zn^{2+} , Cr^{2+} , $\text{V}^{3+}/\text{V}^{4+}$, Ni^{2+} , Co^{2+} , Ga^{2+}) can be incorporated into the magnetite crystal lattice, and their concentrations are a function of fluid and/or magma compositions, oxygen fugacity ($f\text{O}_2$), crystallographic factors, and element partitioning behavior (e.g., Lindsley, 1976; Barnes and Roeder, 2001; Nadoll and Koenig, 2011).

Compositions of magnetite are also affected by the nature of its host rocks and mineral inclusions, as well as by the type and extent of fluid-rock interactions (e.g., Duan et al., 2012, 2014; Hu et al., 2014a,b; Chen et al., 2015; Chung et al., 2015; Liu et al., 2015; Zhao and Zhou, 2015; Wang et al., 2017; Xie et al., 2017; Wu et al., 2019). Therefore, mineral geochemistry has been used to distinguish the magnetite formation environment and metallogenetic types (e.g., Dupuis and Beaudoin, 2011; Dare et al., 2012, 2014; Nadoll et al., 2012, 2014, 2015; Chen and Han, 2015; Liu et al., 2015), and is also a potential exploration vectoring tool for concealed orebodies (e.g., Pisiak et al., 2014, 2017; Canil et al.,

* Corresponding author at: State Key Laboratory of Nuclear Resources and Environment, East China University of Technology, PR China.

E-mail address: lengchengbiao@vip.gyig.ac.cn (C.-B. Leng).

2016).

In porphyry Cu-(Au) systems, magnetite is widely present as an accessory mineral in the porphyries and magnetite-bearing quartz-sulfide veins (e.g., Lowell and Guilbert, 1970; Gustafson and Hunt, 1975; Sillitoe, 2010; Wu et al., 2019). In Fe-(Cu) skarn systems, magnetite commonly occurs as accessory mineral and/or as massive ores, formed via extensive contact metasomatism by magmatic-sourced Fe-rich fluids (e.g., Einaudi, 1981; Meinert, 1987; Meinert et al., 2005). Various discrimination diagrams, such as $(\text{Ni} / (\text{Cr} + \text{Mn}))$ vs. $(\text{Si} + \text{Mg})$ and $(\text{Al} + \text{Ti})$ vs. $(\text{Ti} + \text{V})$, have been proposed to differentiate the magnetite from these two deposit types (e.g., Dupuis and Beaudoin, 2011; Nadoll et al., 2014, 2015). However, it has been suggested that the primary compositions of magnetite are easily modified by later hydrothermal alteration, casting doubts on the reliability of these diagrams (Sidhu et al., 1981; McQueen and Cross, 1998; Cornell and Schwertmann, 2003; Rabbia et al., 2009; Angerer et al., 2012; Wang et al., 2012; Hu et al., 2015; Wen et al., 2017). For instance, primary magnetite can be dissolved and reprecipitated as hydrothermal varieties during later hydrothermal events, and can change the trace element contents (e.g., Ti, Al, Mg, Cr, Mn, Co, Cu and Sn) in the magnetite (Hu et al., 2015; Wen et al., 2017). Sub-solidus processes, such as exsolution of ilmenite lamellae (Frost and Lindsley, 1991), martitization (hematite after magnetite) and/or mushketovitization (magnetite after hematite) (Cornell and Schwertmann, 2003; Angerer et al., 2012), may also alter the original trace element chemistry of magnetite. Therefore, systematic magnetite geochemical studies from typical porphyry and skarn deposits can clarify the magnetite elemental behavior in various magmatic-hydrothermal systems.

A large number of the late Triassic intermediate-felsic porphyries are distributed in the Zhongdian region in northwestern Yunnan (SW China). Some of them are genetically linked to large-/medium-sized Cu-Au deposits (Leng et al., 2012, 2014, 2018), making it an important porphyry and skarn ore belt in China. Magnetite, as a common metallic mineral in these deposits, provides an opportunity to investigate its textural and compositional changes during hydrothermal alteration in these porphyry related deposits. In this study, we investigate the compositional and textural discrepancies of various types of magnetites from the Tumugou (Fm.) andesite and various ore-forming porphyries at the Pulang Cu-Au, Lannitang Au-Cu, and Langdu Cu skarn deposits, and the altered porphyries in the Disuga area. We aim to: (1) determine the controlling factors on the textures and trace element contents of magnetite; (2) suggest new geochemical plots that may help to distinguish different magnetite origins.

2. Geological background

2.1. Zhongdian region

The Zhongdian region is situated in the southern part of the Yidun terrane, which lies between the Songpan-Ganzi and Qiangtang terranes in the eastern margin of the Tibetan Plateau (Hou et al., 2003; Zeng et al., 2003). Exposed sequences in the Zhongdian region are mainly composed of Middle to Upper Triassic clastic and volcanic rocks. The Upper Triassic volcanic-sedimentary sequences were divided into the Qugasi, Tumugou, and Lamaya formations from the bottom to the top (YBGMR, 1999). The Zhongdian region has vast exposure of Late Triassic arc-related andesites and intermediate-felsic porphyries (Leng et al., 2012, 2014). These porphyries were emplaced along an eastern and a western belt, separated by the Hongshan-Rerong Fault (Leng et al., 2012; Wang et al., 2011, 2013a,b). The eastern belt contains the Pulang, Songnuo, Langdu and Disuga plutons, whilst the western belt contains the Lannitang, Xuejiping, Chundu and Ousaila plutons (Fig. 1).

2.2. Pulang porphyry Cu-Au deposit

The Pulang deposit is the largest porphyry deposit in the Zhongdian

region, and has proven metal reserve of ~4.31 million tonnes (Mt) Cu (0.34%) and 113 t Au (0.09 g/t) (Li et al., 2011). Cu-Au orebodies are mostly hosted in the Pulang intrusive complex, which was emplaced into the clastic rocks of Tumugou Formation (Wang et al., 2008) (Fig. 2). The intrusive complex contains five generations of porphyry stocks/dikes, including (from oldest to youngest): quartz diorite porphyry, monzodiorite porphyry, quartz monzonite porphyry, granodiorite porphyry and andesite porphyry (Leng et al., 2018). Alteration styles include potassie, sericite, and propylitic. Potassie alteration occurred in the central part of the alteration zone and is surrounded by propylitic alteration. Both alteration types were locally overprinted by the late sericite alteration. The Cu-Au mineralization is mainly associated with the phyllitic and potassie alteration. Wang et al. (2008) obtained SHRIMP zircon U-Pb ages of 228–226 Ma for the quartz monzonite porphyry, slightly older than the ID-TIMS zircon U-Pb age of 211.8 ± 0.5 Ma for the same porphyry (Pang et al., 2009). The mineralization was dated to be 213 ± 3.8 Ma (Zeng et al., 2006), which falls into the potassie alteration age range (hornblende and biotite $^{40}\text{Ar}/^{39}\text{Ar}$ plateau age: 216–210 Ma) (Li et al., 2011; Zeng et al., 2006). The ores contain a chalcopyrite-pyrrhotite-pyrite assemblage, and fluid inclusions of CO_2 , CO and CH_4 were observed (Liu et al., 2013; Li et al., 2019).

2.3. Langdu Cu skarn deposit

The Langdu deposit is a typical Cu skarn deposit located in the eastern belt (Ren et al., 2013). It contains an estimated reserve of 104 kt of Cu at 6.49% (Li et al., 2009; Ren et al., 2013). The intrusions at Langdu include quartz monzonite porphyry and quartz diorite porphyry, and they were emplaced (ca. 217 Ma) into the sedimentary and volcanic rocks of the Qugasi Formation (Fig. 3) (Zeng et al., 2003). Skarn and hornfels are commonly developed in the intrusive contact of the quartz monzonite porphyry (biotite $^{40}\text{Ar}/^{39}\text{Ar}$ age = 216.9 ± 4.3 Ma; Zeng et al., 2003). Copper mineralization (mineral assemblage: chalcopyrite-pyrrhotite-chlorite-epidote-calcite) occurred in the retrograde skarn stage. The widespread occurrence of pyrrhotite and methane inclusions indicates a relatively reducing ore-forming condition (Ren et al., 2013).

2.4. Lannitang porphyry Au-Cu deposit

The Lannitang deposit is situated in the western belt and has proven reserve of 0.54 Mt Cu (0.38%) and 37 t Au (0.24 g/t). It is mainly hosted in the Lannitang intrusive complex, which is composed of (quartz) diorite and quartz monzonite porphyry and intruded the clastic rocks of Tumugou Formation (Fig. 4). The ore-causative quartz monzonite porphyry is LA-ICP-MS zircon U-Pb dated to be 219.2 ± 1.8 Ma (author's unpubl. data). Alteration zoning is clear at Lannitang, including (from core to rim) the potassie, chlorite-sericite, sericite, propylitic and argillic zones. The potassie alteration is generally overprinted by chlorite-sericite alteration, and the sericite alteration commonly overprints on the chlorite-sericite and potassie alteration. The Cu-Au mineralization is mainly associated with potassie and chlorite-sericite alteration. In the potassie zone, magnetite is present and slightly predates the ore-stage chalcopyrite. In the chlorite-sericite zone, patchy chalcopyrite commonly coexists with gypsum. The widespread oxidized mineral assemblages (magnetite-hematite and anhydrite-gypsum) indicate the oxidation state of the Lannitang ore-forming magma was high (e.g., Sun et al., 2013; Yu et al., 2016).

2.5. Disuga porphyry

The Disuga quartz diorite porphyry is distributed in the eastern belt of this region (Fig. 5). The porphyry intruded the clastic and pyroclastic rocks of the Tumugou Formation between 217 and 203 Ma (Liu et al., 2014; author's unpubl. data), and are intensely phyllitic- to propylitic-

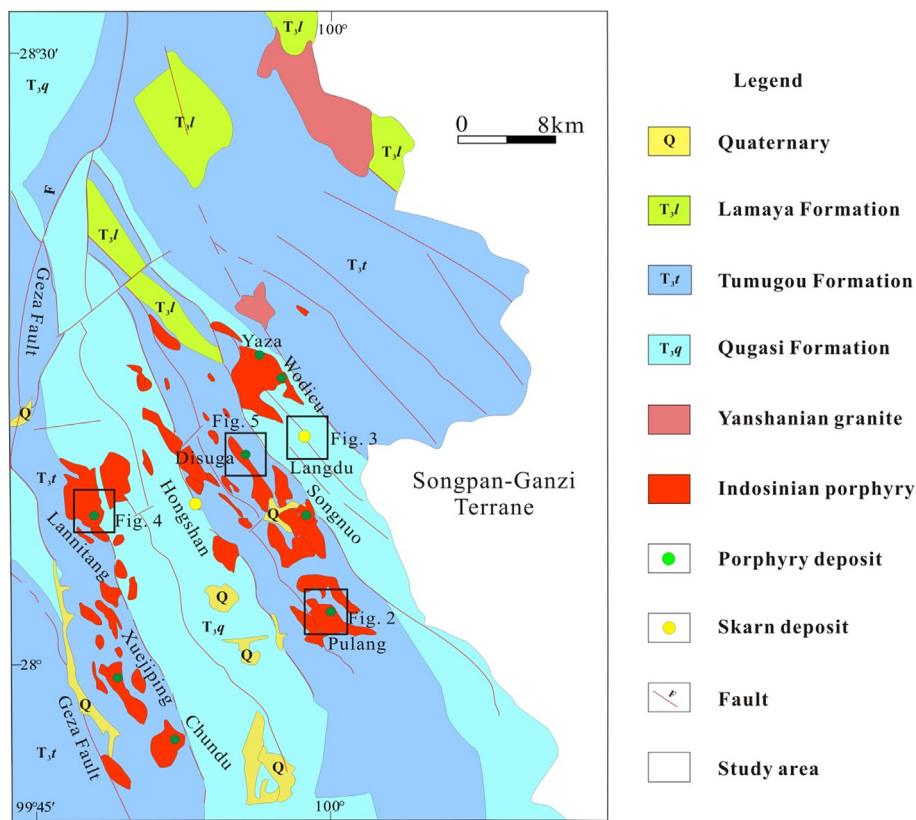


Fig. 1. Simplified geologic map of the Zhongdian region (modified after Leng et al., 2012, 2014).

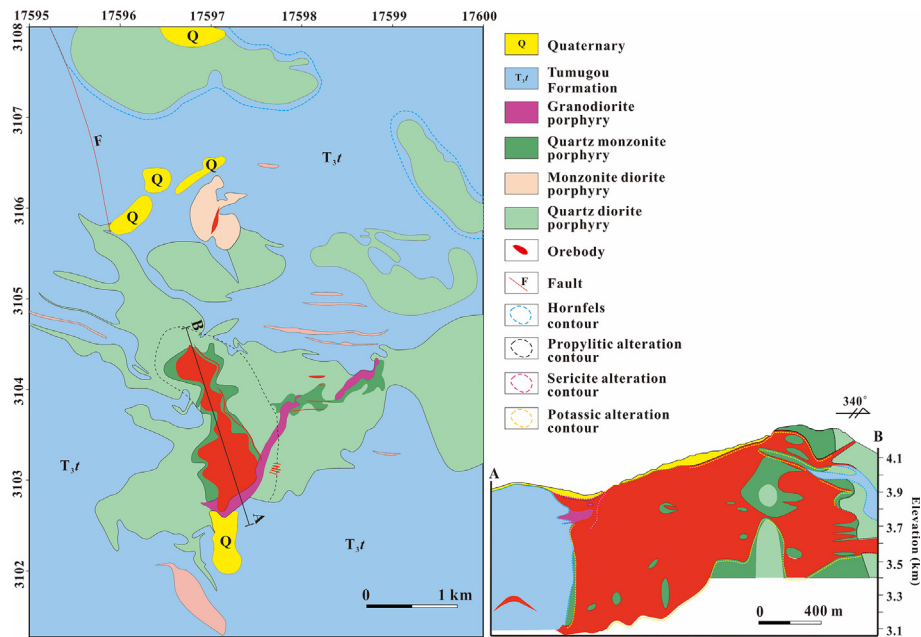


Fig. 2. Geologic map and cross section of the Pulang porphyry Cu-Au deposit (modified after Leng et al., 2018).

altered. Its exposed part is mainly sericite-altered with a small number of chalcopyrite-pyrite-galena-sphalerite veins/veinlets (Liu et al., 2014).

2.6. Andesite of Tumugou Formation

The Upper Triassic Tumugou Formation (Fm.) is widespread in the Zhongdian region. It contains over 2500-m-thick volcanic rocks,

including basalt, andesite, and dacite (YBGMR, 1999). The Tumugou Fm. andesite crops out mainly at Xuejiping and Disuga (Wang et al., 2011). The rocks are generally chlorite-sericite altered and zircon U-Pb dated to be ca. 220 Ma (Leng et al., 2014).

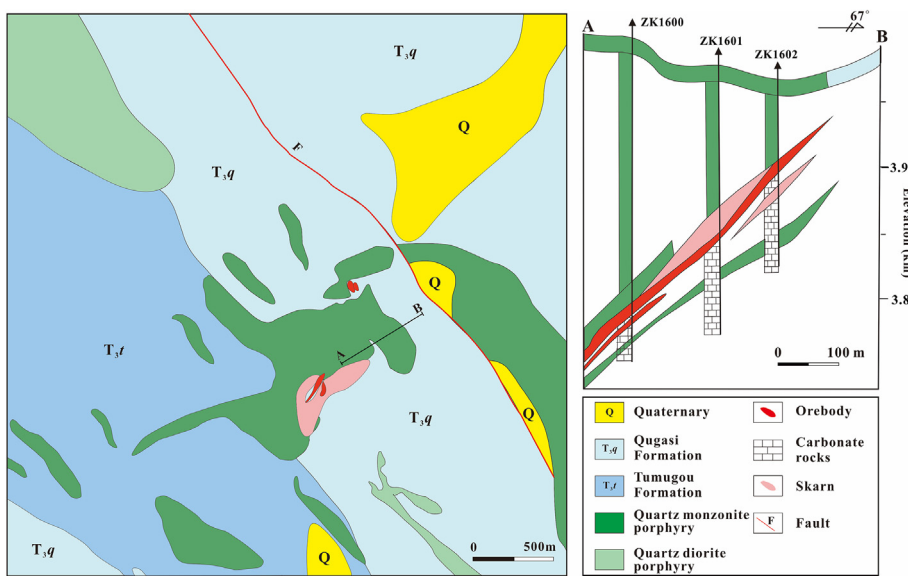


Fig. 3. Geologic map and cross section of the Langdu Cu skarn deposit (modified after Ren et al., 2013).

3. Sampling and analytical methods

3.1. Sampling

Seven magnetite-bearing porphyry samples were collected from the potassic alteration zone of quartz monzonite porphyry body in the Pulang deposit. The quartz monzonite porphyry consists of phenocrysts including plagioclase, amphibole, biotite, and quartz and felsic groundmass, with main accessory minerals of apatite, rutile, and magnetite. The magnetite grains are commonly intergrown with amphibole, biotite and plagioclase (Fig. 6a). Two samples of magnetite-bearing porphyry were collected from the potassically-altered quartz monzonite porphyry body in the Langdu deposit. The magnetite grains coexist with biotite and plagioclase (Fig. 6b). At Lannitang, five magnetite-bearing porphyry samples were collected from the chlorite-sericitic-altered quartz monzonite porphyry. Magnetite grains commonly coexist with hematite (Fig. 6c), or are surrounded by chlorite and sericite (Fig. 6d). Three magnetite-bearing samples were collected from the sericitic-altered quartz diorite porphyry at Disuga. Magnetite grains commonly coexist with partly chloritized biotite and sericitized plagioclase (Fig. 6e). Three andesite samples from outcrops of the Tumugou

Formation were also collected. These andesite samples are generally chlorite-sericitic altered as the original mafic minerals and plagioclase crystals were replaced by pseudomorphic chlorite and sericite, respectively. Magnetite grains are disseminated in the altered andesite (Fig. 6f).

3.2. SEM-BSE

All specimens were prepared into polished thin sections and inspected by optical microscopy and back-scattered electron (BSE) imaging to reveal their mineral and textural features. BSE imaging was performed using a JSM-7800 thermal field Scanning Electron Microscope (SEM) connected with an EDAX Energy Dispersive Spectrometer (EDS) in the State Key Laboratory of Ore Deposit Geochemistry (SKLODG), Institute of Geochemistry, Chinese Academy of Sciences. SEM-EDS mapping was conducted using a 20nA beam current, 25 kV accelerating voltage and 1000 ms/step counting time.

3.3. EPMA

Magnetite was analyzed using an EPMA-1600 electron microprobe

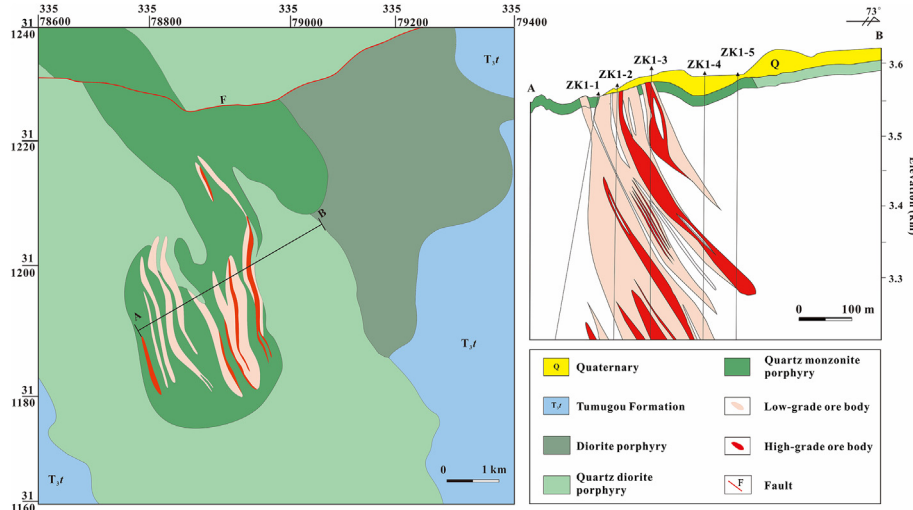


Fig. 4. Geologic map and cross section of the Lannitang porphyry Au-Cu deposit.

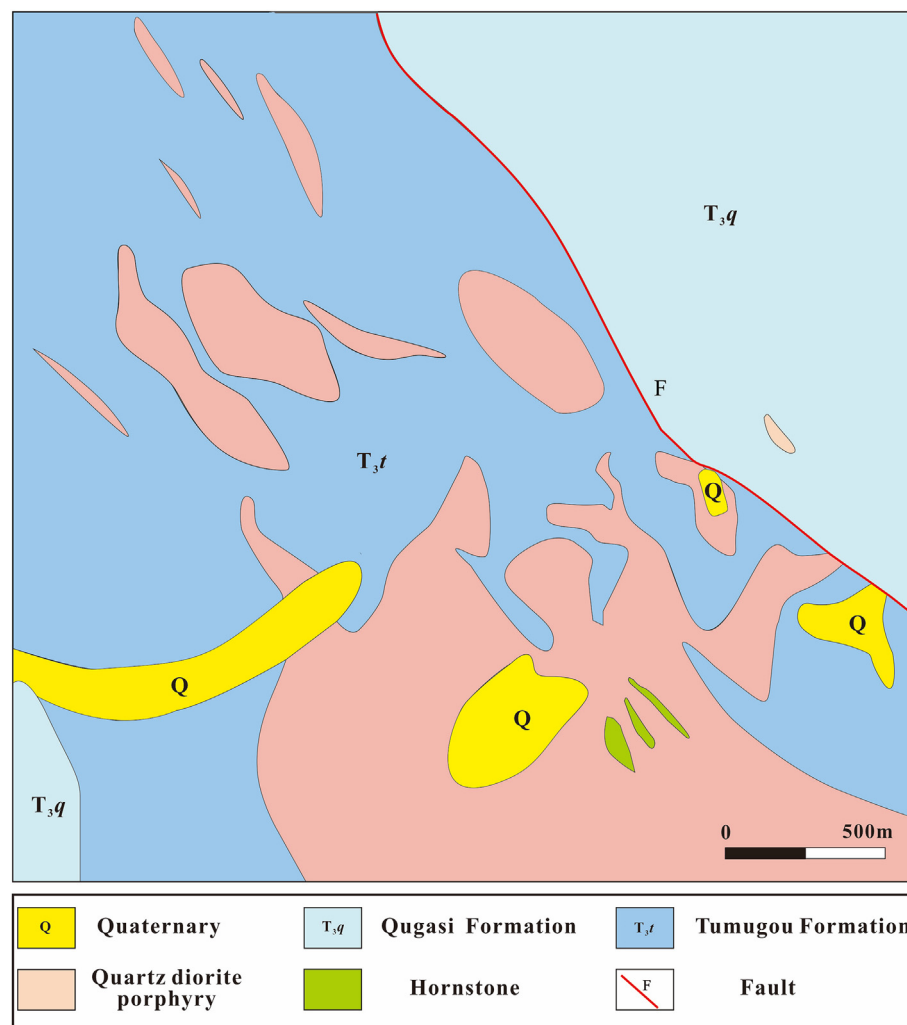


Fig. 5. Geologic map of the Disuga porphyry (modified after Liu et al., 2014).

at SKLODG. The analysis was conducted under 10 nA current, 25 kV voltage and 10 μm spot size. For major elements, peak and background counting times were set to 20 s and 10 s, respectively, and 40 s and 20 s for trace elements. Magnesium, Ca, Ti and Fe were measured by a focused beam (1 μm) at 25 kV and 20nA. For the Wave Dispersive Spectrometer (WDS) analyses, the standards used were: Fe (magnetite), Ti (rutile), Mg and Ca (garnet).

3.4. LA-ICP-MS

The LA-ICP-MS analysis was conducted using a 193 nm ArF excimer laser ablation system (GeoLas Pro) coupled with an Agilent 7700x ICP-MS in the SKLODG. Argon was used as the make-up gas and mixed with the carrier gas through a T-connector before entering the ICP. The ablated material was transported in He carrier gas to a modified glass mixing bulb where they were mixed coaxially with Ar prior entering into the ICP torch. The analysis used 32 μm laser spot size, 10 Hz frequency, and 6 J/cm² energy density. BCR-2G, GSE-1G, BIR-1G, BHVO-2G and NIST610 were used as external standards and ⁵⁷Fe as internal standard to calibrate the elemental contents (Liu et al., 2008; Nadoll and Koenig, 2011; Huang et al., 2013). Each measurement includes a background of 15 s (gas blank) followed by 60 s of sample data acquisition. Quality control of time-dependent drift of sensitivity and mass discrimination was monitored by analyzing GSE-1G for every five analyses. Trace elements calibration was performed with ICPMSDataCal (Liu et al., 2008).

The isotopes of ²⁷Al, ²⁹Si, ³¹P, ⁴⁴Ca, ⁴⁵Sc, ⁴⁷Ti, ⁵¹V, ⁵³Cr, ⁵⁵Mn, ⁵⁷Fe, ⁵⁹Co, ⁶⁰Ni, ⁶³Cu, ⁶⁶Zn, ⁷¹Ga, ⁷⁴Ge, ⁸⁸Sr, ¹¹⁸Sn, ²⁰⁸Pb, ²³²Th and ²³⁸U were measured in the analysis. The isotopes of ²⁷Al, ²⁹Si, ³¹P, ⁴⁴Ca, ⁶³Cu, ⁸⁸Sr, ²⁰⁸Pb, ²³²Th and ²³⁸U were used to detect the mineral inclusions. The mineral inclusions, including those of sulfides, silicates and apatite, were detected in this study (see below). Signal anomalies (e.g., spikes) were screened out visually for mineral heterogeneities (e.g., micro-inclusions and compositional zoning) to ensure data integrity.

4. Magnetite I and II

Based on petrographic and mineral textural observations (Figs. 6, 7), we have divided the magnetite grains into two groups, i.e., Magnetite I and II. Magnetite I grains commonly coexist with chlorite, rutile and titanite (Fig. 7a–c), and some contain apatite inclusions (Fig. 7b). Magnetite I grains generally contain porous cores and homogeneous rims, both of which have sharp contacts (Fig. 7e). A few fine ilmenite lamellae (commonly < 1 μm) were also observed in the cores of some Magnetite I grains (Fig. 7d). Magnetite I is commonly distributed in the chlorite-sericite and sericite alteration zones (at Lannitang, Disuga porphyry and Tumugou Fm. andesite). Magnetite II grains are texturally homogeneous and imporous. The rutile coexists with Magnetite II (Fig. 7f–h). Magnetite II grains are distributed in various alteration zones. Some are distributed in the potassic alteration zone of the Pulang and Langdu deposits, and minor in the sericite alteration zone (at

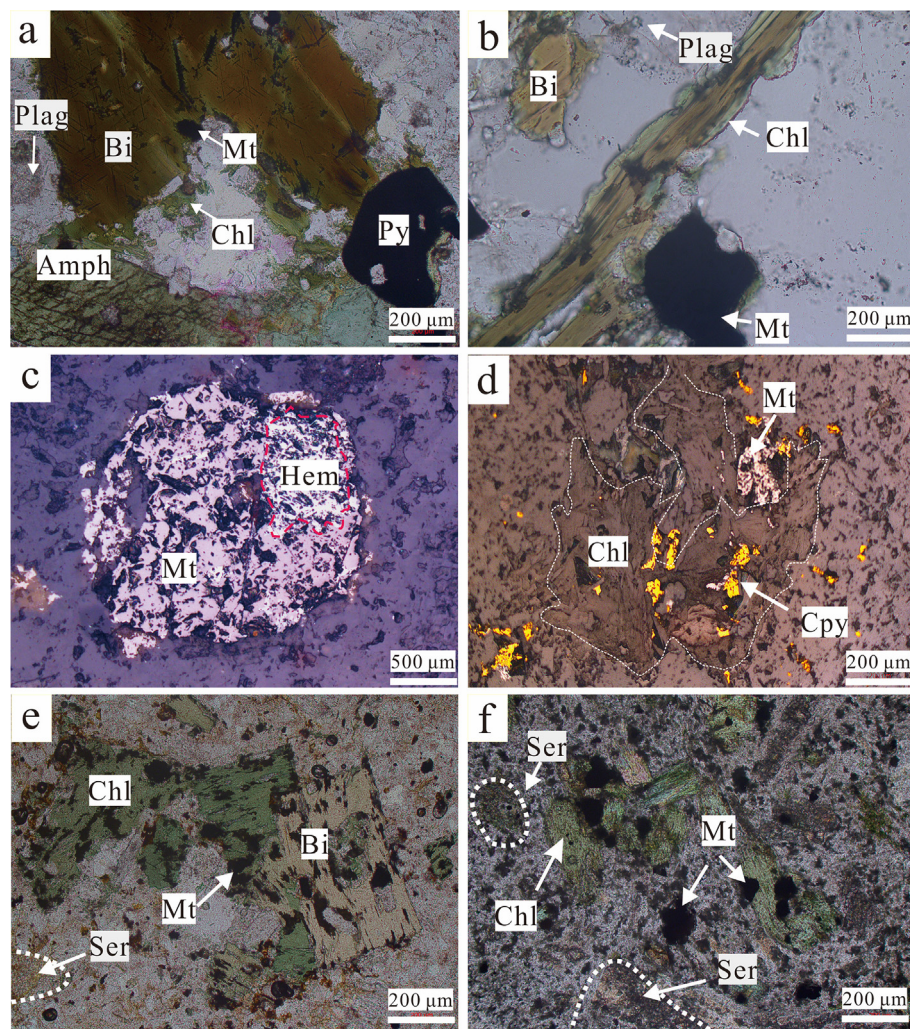


Fig. 6. Microphotographs of representative magnetite samples from the Zhongdian region. (a) Magnetite in the Pulang deposit. The magnetite is intergrown with biotite, chlorite, amphibole, and plagioclase; (b) Magnetite from the Langdu deposit. The magnetite is intergrown with biotite, chlorite, and plagioclase; (c) Magnetite is intergrown with hematite (Lannitang); (d) Magnetite coexists with chlorite and followed by chalcopyrite (Lannitang); (e) Magnetite from the porphyry at Disuga. Biotite are partially altered to chlorite and plagioclase to sericite; (f) Magnetite from the Tumugou Fm. andesite. Biotite and plagioclase altered to chlorite and sericite, respectively. Abbreviations: Amph-amphibole; Bi-biotite; Chl-chlorite; Cpy-chalcopyrite; Hem-hematite; Mt-magnetite; Plag-plagioclase; Py-pyrite; Ser-sericite.

Lannitang and Disuga porphyry).

In the Pulang intrusive complex, the magnetite is dominantly euhedral-subhedral and 20–200 μm long (Fig. 6a). BSE imaging shows that the magnetite is texturally homogeneous, bright and essentially imporous, belonging to Magnetite II (Fig. 7g). The magnetite is commonly surrounded by rutile (Fig. 7g). The magnetite grains from Langdu are dominantly euhedral (20–100 μm long), textually homogeneous and belong to Magnetite II (Figs. 6b, 7h). These samples are collected from potassic-altered porphyries of Pulang and Langdu deposits.

Both Magnetite I and II are found in the samples from Lannitang and Disuga. They are dominantly euhedral-subhedral and 10 to 100 μm long. Some grains (i.e., Magnetite I) contain porous core with smooth grain boundary (Fig. 7a, e), whereas others (i.e., Magnetite II) are texturally homogeneous (Fig. 7f). Ilmenite lamellae are also present in the core of Magnetite I (Fig. 7a, e). Magnetite I is commonly intergrown with chlorite and rutile (Fig. 7a). The surrounding biotite and amphibole are altered partially to chlorite (Fig. 6e), and plagioclase to sericite (Fig. 6e). Magnetite II grains in Lannitang and Disuga are generally intergrowth with quartz and plagioclase (Fig. 6d, e). The plagioclase was altered to sericite. These grains are mainly distributed in the chlorite-sericite (Lannitang) and sericite (Disuga) alteration zones.

In the Tumugou Fm. andesite, the magnetite grains are all euhedral-subhedral Magnetite I. They are 10 to 80 μm long, and have porous core and smooth rims (Fig. 7b-c). The magnetite grains are commonly intergrown with chlorite, rutile and titanite (Fig. 7b-c). These samples experienced intense sericite alteration. The biotite and amphibole are

completely altered to chlorite (Fig. 6f), and feldspars to sericite.

5. Results

5.1. EPMA and SEM-EDS mapping

Fifty-nine magnetite grains were analyzed using EPMA to determine their major elements compositions (Table 1). Overall, the FeO contents range from 88.72 to 94.75 wt% (mean 92.3 wt%), the TiO₂ are highly variable (from below the detection limit (BDL) to 5.01 wt%). Magnetite from the Tumugou Fm. andesite contains the highest TiO₂ (up to 5.01 wt%), whereas most magnetite at Pulang has TiO₂ contents close to or below BDL. In addition, all the analyzed magnetite samples contain minor MgO (from BDL to 0.18 wt%) and CaO (from BDL to 0.15 wt%) (Table 1).

SEM-EDS mapping was used to reveal elemental distribution patterns of Magnetite I. The results, verified by the subsequent EPMA analysis, suggest that the Ti content decreases from core to rim (Fig. 8). As shown in Fig. 9a, the TiO₂ content decreases from 2.13 wt% in the core to 0.15 wt% at the rim, whereas the corresponding FeO content increases from 91.84 to 93.86 wt%. In Fig. 9b, the atomic weight of iron increased from 43.26 to 45.92 (Fig. 9b).

5.2. LA-ICP-MS trace element

Seventy-four spot analyses were performed on the magnetite grains from 21 samples (Table 2). We only analyzed the core of Magnetite I as

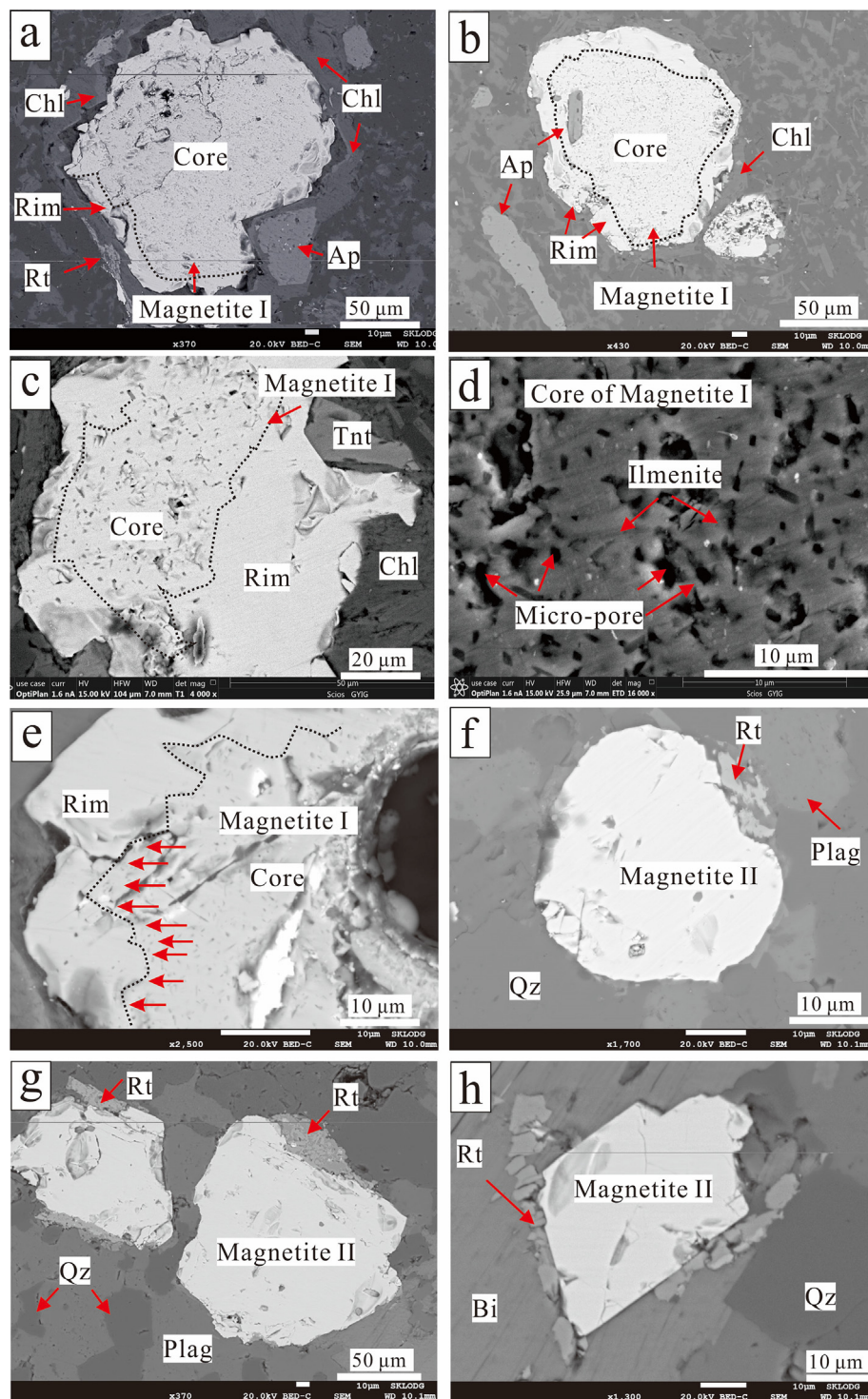


Fig. 7. BSE (back-scattered electron) images of magnetite grains from the Zhongdian region. (a) Porous-core and homogeneous-rim texture of Magnetite I. It coexists with rutile, chlorite and apatite from the Disuga porphyry; (b) Magnetite I with apatite inclusions from the Tumugou Fm. andesite. It has porous core and homogeneous rim; (c) Magnetite I is intergrown with chlorite and titanite. Magnetite I has porous core and homogeneous rim in the Tumugou Fm. andesite; (d) High-contrast and high-resolution image of the Magnetite I core; (e) Porous Magnetite I core in sharp contact with the magnetite rim (arrow) (Lannitang); (f) Magnetite II from the porphyry at Disuga; (g) Magnetite II is intergrown with rutile, plagioclase and quartz (Pulang); (h) Magnetite II from Langdu coexists with biotite and rutile. Abbreviations: Qz-quartz; Rt-rutile; Tnt-titanite; others are as in Figure 6.

the rim is too narrow (thinner than the laser beam diameter) to be analyzed. The maximum, minimum (95% confidence intervals) and calculated average values of selected elements in the core of Magnetite I and Magnetite II are presented in Fig. 10, and the multi-element spider diagram is shown in Fig. 11 (normalized to the mean values of Magnetite II).

The core of Magnetite I (Lannitang deposit, Disuga porphyry and Tumugou Fm. andesite) commonly has higher Ti and Sc than Magnetite II (Pulang, Langdu, Lannitang deposits and Disuga porphyry). The Cr and Ga concentrations in the core of Magnetite I are generally lower than those of Magnetite II. These trends are found between Magnetite I

and II not only from different deposits, but also within a single deposit (e.g., at Lannitang deposit and at Disuga porphyry) (Figs. 11, 12).

According to Table 2, the magnetite in the Tumugou Fm. andesite contains the highest concentrations of Sc ($\text{mean} \pm \sigma = 2.79 \pm 2.57 \text{ ppm}$), Ti ($30,347 \pm 6449 \text{ ppm}$), Pb ($24.6 \pm 52.1 \text{ ppm}$), and the lowest Ga ($2.01 \pm 0.46 \text{ ppm}$), V ($756 \pm 86 \text{ ppm}$), and Zn ($15.7 \pm 2.90 \text{ ppm}$) concentrations among the analyzed magnetite samples (Table 2). Meanwhile, the Pulang magnetite has the highest concentrations of V ($2561 \pm 812 \text{ ppm}$), Ga ($11.8 \pm 6.97 \text{ ppm}$), and the lowest Sn ($0.15 \pm 0.13 \text{ ppm}$). The Disuga magnetite contains the highest Zn ($51.9 \pm 56.2 \text{ ppm}$), whereas the Langdu magnetite has the

Table 1

EPMA results of major and trace elements (wt%) of the magnetite from various igneous rocks in the Zhongdian region.

Sample	MgO	TiO ₂	FeO _T	CaO	Fe ₂ O ₃ *	FeO*
<i>Pulang (Type II)</i>						
PLZK04046-297-1	0.06	0.02	90.6	0.09	63.0	35.9
PLZK04046-297-2	0.06	0.02	89.7	0.09	64.4	32.8
PLZK04046-297-4	0	0.1	93.7	0.02	57.8	46.9
PLZK04046-297-5	0.02	0.02	92.6	0.09	59.8	42.8
PLZK04046-297-6	0	0	92.4	0.1	60.2	42.0
PLZK04046-297-7	0.15	0.01	89.2	0.18	65.0	31.5
PL1416-747-1	0.02	0.08	94	0	57.4	47.9
PL1416-747-2	0.02	0	93	0.01	59.3	43.9
PL1416-747-3	0	0	94.6	0.02	56.6	49.8
PL1416-747-4	0	0	94.7	0.04	56.3	50.2
PL1416-747-5	0.03	0	93.9	0	57.8	47.2
PL1416-747-6	0.01	0.01	94.5	0.01	56.7	49.4
PL1416-747-7	0.03	0.04	93.5	0.02	58.3	46.0
PL1416-747-8	0.04	0.03	92.8	0.03	59.5	43.5
PL1416-747-9	0.02	0	93.3	0.08	58.7	45.3
PL1416-747-10	0	0.04	93.3	0.12	58.5	45.5
PL1416-747-11	0.02	0.02	92.1	0.06	60.7	41.0
PL1416-747-12	0.03	0.06	92.1	0.07	60.5	41.2
PL302-6-1	0.02	0.09	91.7	0.06	61.1	39.8
PL302-6-2	0	0.12	92.1	0.15	60.1	41.6
PL302-6-3	0.01	0.03	91.9	0.06	61.0	40.3
PL302-6-4	0	0	92.7	0.02	59.8	42.8
PL302-6-5	0	0.01	93	0.02	59.3	44.0
PL302-6-6	0.01	0.02	92.8	0.01	59.6	43.3
PL302-6-7	0	0.05	92.5	0.02	60.0	42.3
PL302-6-8	0.01	0	92.8	0.01	59.7	43.2
PL302-6-9	0	0.05	91.7	0.05	61.2	39.6
PL12-26-1	0.05	0.09	91.8	0.02	61.0	40.1
PL12-26-2	0.02	0.13	91.6	0.03	61.2	39.5
<i>Langdu (Type II)</i>						
LD07-47-1	0	0.06	91.3	0.06	61.8	38.3
LD07-47-2	0.01	0.05	91.3	0.04	61.9	38.2
LD07-47-3	0	0.03	91.7	0.05	61.3	39.5
LD07-47-4	0	0.03	88.7	0.08	65.9	29.3
LD07-47-5	0	0.03	89.9	0.07	64.1	33.3
<i>Lannitang (Type II)</i>						
3-7-15-1	0.02	0.62	93.6	0	56.1	48.7
3-7-15-2	0.01	1.04	91.5	0.03	58.1	42.9
3-7-15-3	0.08	0.78	90.1	0.06	61.2	37.2
3-7-15-4	0.04	0.33	92.1	0.02	59.6	42.2
3-7-15-5	0.01	0.22	92	0.02	60.2	41.3
3-7-15-6	0	0.31	93.2	0.02	57.9	46.0
3-7-15-7	0.03	0.26	92.9	0.01	58.6	44.7
3-7-15-8	0.01	0.56	92.9	0.11	57.3	46.2
<i>Disuga (Type II)</i>						
DSG11-25-1	0.03	0.02	92.3	0.03	60.4	41.6
DSG11-25-2	0.01	0.1	94	0.04	57.2	48.1
DSG11-25-3	0.02	0.81	93.1	0.02	56.2	47.8
DSG11-25-4	0	0.12	94.1	0.03	57.0	48.5
'DSG11-25-5	0.03	0.08	93.1	0.06	58.8	44.8
DSG11-25-6	0.02	0.24	93.5	0.1	57.4	47.1
DSG11-25-7	0	0.36	94	0.03	56.3	49.1
<i>Tumugou Fm. andesite (Type I)</i>						
DSG11-31-1	0.01	5.01	89.3	0.03	47.4	51.7
DSG11-31-2	0.03	0.75	92.6	0.22	56.8	46.4
DSG11-31-3	0.04	0.19	91.4	0.2	60.9	39.7
DSG11-31-4	0	0.38	90.3	0.24	62.0	36.6
DSG11-31-5	0	1.34	90.6	0.05	58.5	41.0
DSG11-31-6	0.02	0.41	93.3	0.08	57.2	47.0
DSG11-31-7	0	2.13	91.8	0.04	53.6	48.6
DSG11-31-8	0	0.15	93.9	0.1	57.1	48.1
DSG11-31-9	0	3.97	90.9	0	48.4	53.0
DSG11-31-10	0	3.52	92	0.03	48.0	55.3

*Contents of Fe₂O₃ and FeO are calculated based on 4 oxygens.

highest Mn (380 ± 117 ppm), Cr (1281 ± 80.3 ppm), and Ni (62.4 ± 33.9 ppm), and the lowest Pb (0.12 ± 0.18), Al (80.4 ± 38.9 ppm), Ge (0.53 ± 0.16), Sc (0.16 ± 0.13 ppm), Ti (21.6 ± 24.5 ppm), and Mg (21.7 ± 24.5 ppm). The Lannitang

magnetite has the highest Al (1984 ± 1746 ppm), Ge (2.84 ± 0.84 ppm), and Mg (1121 ± 1987 ppm), and the lowest Mn (11.8 ± 10.8 ppm), Cr (143 ± 95.3 ppm), and Co (15.4 ± 6.39 ppm). Over 65% of the magnetite grains contain < 5 ppm of Cu (Table 2).

5.3. Mineral inclusions in magnetite

The LA-ICP-MS signals record the elemental variations with the deepening of the laser ablation hole. Four representative signal spectra are shown in Fig. 13. The spectra in Fig. 13a show flat signal lines of Fe, Ti, V, and Mn, indicating that these four elements can be incorporated into the crystal lattice of magnetite. There are some spectral spikes on Al, Ca, Zr, Th, U, Cr, Sr, Mn, Cu, and S in the other three images (Fig. 13b-d), which could be caused by micro-inclusions of minerals including zircon and/or other silicates and sulfides (e.g., chalcopyrite, pyrite). The magnetite at Pulang hosts many types of mineral inclusions, such as zircon, and other silicates (Fig. 13b). No sulfide inclusions are found in the samples from Pulang and Langdu deposits. The magnetite from the Tumugou Fm. andesite generally contains apatite and silicate inclusions (Fig. 13c). Additionally, a few sulfide inclusions were identified in magnetite at Lannitang and Disuga (Fig. 13d). Data with possible mineral heterogeneities (e.g., inclusions or zoning) were visually removed and not discussed here.

6. Discussion

6.1. Origin of Magnetite I and dissolution-reprecipitation process

Magnetite I is characterized by being textually inhomogeneous due to its porous core and homogeneous rim. The core (with local ilmenite exsolution lamellae) of Magnetite I is rich in Ti (average 16,646 ppm) and Cr (average 392 ppm), indicative of a dominantly igneous origin (Buddington and Lindsley, 1964; Ghiors and Sack, 1991; White et al., 1994; Dupuis and Beaudoin, 2011; Dare et al., 2014). The primary igneous magnetite and its surrounding biotite, amphibole and plagioclase may have altered to form Magnetite I and its surrounding Ti-rich minerals (titanite and rutile), chlorite and sericite (Rui et al., 1984; Rabbia et al., 2009; Rabbia, 2012; Sillito, 2010).

The hydrothermal alteration results in the dissolution-reprecipitation process in Magnetite I. Dissolution-reprecipitation refers to the process in which the previous assemblages are substituted by more stable ones during physicochemical condition changes (Boulvais et al., 2007; Geisler et al., 2007; Pecoits et al., 2009; Kaur et al., 2012). This is generally triggered by changes in temperature, salinity, and oxygen fugacity of the fluids (Hemley and Hunt, 1992; Hu et al., 2014b). Dissolution-reprecipitation processes commonly develop micro-pores, which allow more fluid access to the reaction interface and provide the mass required for the further process within the crystal (Putnis, 2005, 2009). It may also form irregular grain boundaries via mass and volume changes (Putnis, 2005). For Magnetite I, the presence of numerous micro-pores of the core, the sharp contact between the core and newly-formed epitaxial rim (Fig. 7e; contact marked by arrow), and its irregular grain boundaries altogether suggest the occurrence of dissolution-reprecipitation processes. Once chemical equilibrium between the interfacial fluid and the original magnetite grains was established, continued textural features (i.e., the non-porous, homogeneous Magnetite I rim) were formed (Fig. 7a-c, e; Putnis, 2005; Wen et al., 2017).

In addition, dissolution-reprecipitation is also a chemical purification process (Geisler et al., 2007). Previous studies revealed that many trace elements (e.g., Al, Mg, Ca, Ti, Mn, Zn, Cr, Ga and Sn) would decrease in primary magnetite during dissolution and reprecipitation (Hu et al., 2015; Wen et al., 2017). Wen et al. (2017) proposed that the replacement of igneous magnetite by hydrothermal varieties has led to a loss of 0.77–1.53 wt% Ti, 0.82–1.82 wt% Al, 0.14–0.42 wt% Mg, 0.06–0.3 wt% Mn, and 0.01–0.1 wt% Cr, coupled with an increase of

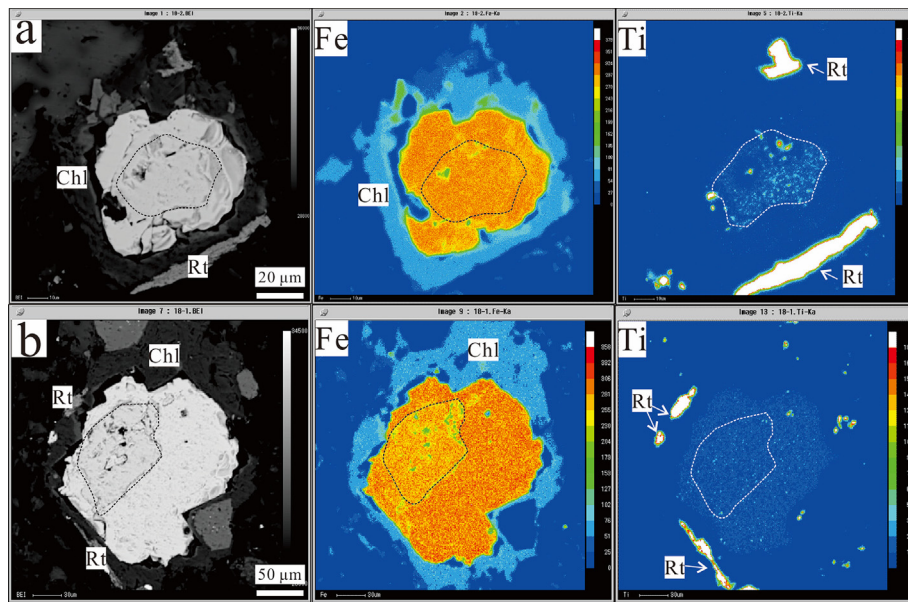


Fig. 8. SEM-EDS mapping of Magnetite I grains from the andesite rocks of Tumugou Formation and the Disuga porphyry, respectively. (a) Under high resolution, the magnetite Ti content decreases from the core to the rim, whereas no discernible core-rim composition zoning for Fe and other trace elements are found (DSG11-31); (b) Under low resolution, two generations of magnetite is clear, with the darker area being the parent magnetite. The Fe content increases from core to rim, suggesting dissolution and reprecipitation (DSG11-18).

1.92–3.38 wt% Fe. As revealed by our SEM-EDS mapping and EPMA analyses (Figs. 8–9; Table 1), the Magnetite I core contains higher Ti (0.19–1.93 wt%) but lower Fe (1.1–3.3 wt%) than its rim. The core-rim variation of other elements (e.g., Al, Mg, Ca, Mn, Cr, Ga, Sn and Pb) of Magnetite I is unknown, either because the rims are too narrow to be analyzed, or their contents are below the EPMA detection limits.

6.2. Origin of Magnetite II and oxygen fugacity in different deposits

Magnetite II is textually homogeneous and has low average contents of Ti (520 ppm), Mg (523 ppm), Al (456 ppm), V (2283 ppm) and Ni (55 ppm), resembling hydrothermal magnetite in porphyry-type deposits (e.g., Dupuis and Beaudoin, 2011; Nadoll et al., 2014; 2015). Hence, we suggest that Magnetite II and its coexisting rutile were both formed by hydrothermal alteration.

The trace element compositions in hydrothermal magnetite (Magnetite II) may reflect the hydrothermal fluid conditions. Some redox-sensitive elements (e.g., Mn and V) in Magnetite II may indicate the relative oxygen fugacity among different types of porphyry-related deposits (Lannitang porphyry Au-Cu, Pulang porphyry Cu-Au, and

Langdu Cu skarn deposits). Mn²⁺ and V³⁺ (rather than Mn⁴⁺ and V⁴⁺, respectively) are more easily incorporated into the magnetite lattice under low $f\text{O}_2$ (Toplis and Corrige, 2002). Yang (1982) proposed that Fe³⁺ is more readily substituted by Sn⁴⁺ (rather than Sn²⁺) under oxidizing conditions. In previous studies, the zircon Ce⁴⁺/Ce³⁺ and δEu values of the Lannitang quartz monzonite porphyry indicate high oxidation state (up to the hematite-magnetite buffer) (Yu et al., 2016). The widespread oxidized mineral assemblages (magnetite-hematite and gypsum) also confirmed high $f\text{O}_2$ ore-fluids at Lannitang. It is well accepted that the ore-fluid $f\text{O}_2$ of Au-rich porphyry Cu deposits is higher than that of gold-poor ones (Oyarzún et al., 2001; Li et al., 2006; Li et al., 2007). Moreover, the occurrence of methane inclusions and pyrrhotite from the Langdu and Pulang deposits indicate their relatively reducing ore-forming environment (Li et al., 2019; Liu et al., 2013). Compared to Magnetite II from Pulang and Langdu, Magnetite II from Lannitang has lower Mn and V contents but higher Sn content (Fig. 14a, c), indicative of higher oxygen fugacity.

Our results suggest that the concentrations of some redox-sensitive elements (Mn, V, and Sn) in Magnetite II can serve as redox indicators for the Lannitang, Pulang and Langdu porphyry-type systems. This

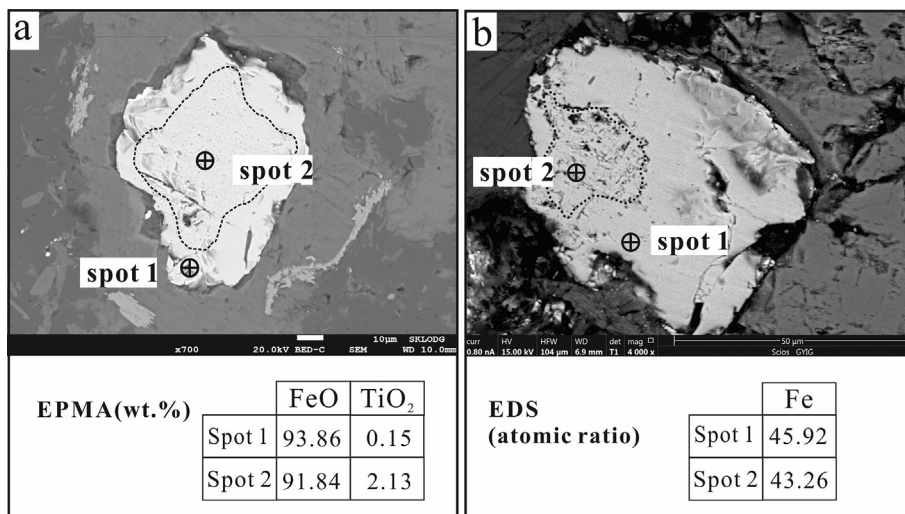


Fig. 9. (a) EPMA data of Magnetite I from the Tumugou Formation andesite (DSG11-18); (b) EDS data of Magnetite I from the Lannitang deposit (ZK1-2-6). Highlight the variation of FeO: TiO₂ (wt%) and Fe (atomic weight).

Table 2

LA-ICP-MS results of trace elements (ppm) of the magnetite from various igneous rocks in the Zhongdian region.

Samples	Mg	Al	Ca	Sc	Ti	V	Cr	Mn	Co	Ni	Cu	Zn	Ga	Ge	Sn	Pb
<i>Pulang (Type II)</i>																
PL0416-286.8-02	30.6	100	51	0	66.8	2974	1044	295	4.09	126	0.38	23.1	8.16	0.94	0.24	0.02
PL0416-286.8-04	35.5	95.9	91	0	13.3	3385	1816	463	20.5	101	0.18	40.6	23.4	0.71	0.18	0.04
PL0416-286.8-05	445	424	15,281	0.1	30	3054	2819	320	25.3	71.9	41.6	30.6	13.9	0.88	0.2	2.57
PL0416-297.5-03	78.9	441	8471	0.72	1342	3960	1459	225	30.4	41.2	4.29	34.7	24.7	1.22	0.54	0.39
PL0416-747-01	220	106	475	0.08	26.7	2273	875	248	16.7	95	1.76	23	21.4	0.73	0.07	2.39
PL0416-747-02	44.2	64.1	1076	0	18.7	993	1076	145	0.93	34.8	1.77	7.91	3.77	1.03	0.14	0.84
PL0416-747-03	20.7	80.2	33	0.1	28.3	1794	963	140	15.5	38.6	0.58	6.19	5.86	1.25	0.3	0.13
PL0416-747-04	21.4	52.2	64	0.07	19.9	1707	1093	150	14.8	39.7	0.46	7.65	5.91	0.87	0.04	1.24
PL0416-747-05	24.1	83.7	47	0.17	29.4	2469	873	230	16.1	49.1	0.22	11.2	13.4	0.94	0.07	0.07
PL0416-835-01	1848	1389	585	1.05	160.5	1774	539	218	0.93	318	59.6	15.6	9.34	0.49	0	9.15
PL0416-835-02	467	227	377	0.82	366.5	3397	48.2	245	1.13	40.4	156.9	17.1	9	1.66	0.19	5.4
PL0416-835-06	40.3	961	281	0.2	585.4	2938	614	285	10.6	8.96	0.5	16.3	26.6	0.99	0.29	0.64
PL0416-835-13	32.8	85.6	259	0.06	21.9	2280	2018	336	17.4	32.4	0.75	16.3	12.8	0.7	0	0.88
PL1208-1039-01	77.9	200	246	0.07	203.1	3705	1168	146	13.2	8	0.56	42.8	23.3	0.93	0.12	0.17
PL1208-1039-02	96.7	195	449	0.14	102.7	3786	1616	122	6.6	20.4	0.64	17.6	16.3	1.31	0.18	0.32
PL302-2-01	37.9	62	128	0.18	32.6	2830	1585	137	32.1	58.7	1.79	22.2	8.14	1.48	0	0.04
PL302-6-01	37.2	66.5	0	0.02	20.3	2909	1016	108	48.2	62.6	0.17	25.8	9.87	0.65	0.13	0.02
PL302-6-03	44.4	59.2	50	0.02	13.4	3753	637	146	37.9	72.1	8.93	35.6	10.5	1.27	0.05	0.21
PL302-6-06	34.2	52.6	41	0.13	18.2	2352	249	91.8	40.2	48.8	98.8	18.3	5.39	1.49	0.13	0.17
PL302-6-09	36.7	59.1	63	0.07	13	1556	543	61.3	22.1	38.2	10.2	13.2	2.99	0.72	0.23	0.07
PL302-6-10	36.7	65.4	0	0.12	11	2362	786	93.7	30.6	40.4	13.7	14.1	5.79	0.82	0.04	0.01
PLE004-460-02	67.5	92.1	2143	0	17.6	1940	184	241	11.4	28.9	0.55	27.8	9.44	1.09	0	4.76
PLE004-460-04	1145	1405	1661	0	116.6	1678	323	159	9.29	20.3	0.31	18.2	9.28	0.92	0.15	4.51
PLE004-460-06	210	227	67	0.26	104.2	2431	800	174	13.7	39.3	0.77	13.5	5.6	0.95	0.39	2.51
PLE004-460-09	33.7	134	1306	0.06	22.9	1732	351	174	14.3	31.5	3.28	22.6	10.0	1.51	0	13.0
Mean	207	269	1330	0.18	135	2561	980	198	18.2	58.7	16.3	20.9	11.8	1.02	0.15	1.98
S.D.	419	391	3369	0.27	284	812	639	92.3	12.6	60.9	37.3	10	6.97	0.3	0.13	3.23
<i>Langdu (Type II)</i>																
LD07-47-01	21.7	125	64	0	49.8	2932	1190	245	45	102	0.63	38.8	17.82	0.37	0.36	0.32
LD-15-03	26.1	59.5	63	0.24	5.87	1611	1340	462	19.3	41.7	0.5	24.9	3.83	0.56	0.22	0.02
LD-15-04	20.6	56.5	139	0.23	9.24	1477	1314	431	19.1	44	0.63	24.6	4.23	0.68	0.19	0.01
Mean	22.8	80.4	89	0.16	21.6	2007	1281	380	27.8	62.4	0.59	29.4	8.63	0.53	0.25	0.12
S.D.	2.9	38.9	44	0.13	24.5	804	80.3	117	14.9	33.9	0.07	8.1	7.96	0.16	0.09	0.18
<i>Lannitang (Type I)</i>																
4-7-9-1-01	980	2044	459	4.91	5675	623	3.3	27.1	23.2	24	0.19	75.7	4.15	2.76	8.62	1.05
4-7-9-1-02	18	59	50	0.58	5364	663	131	1.17	20.3	21.1	0.33	47.2	3.21	2.19	7.06	5.55
4-7-9-1-04	291	226	0	0.5	5475	566	3.84	20.8	20.2	28.8	2.91	37.8	3.28	2.11	6.25	5.83
4-7-9-1-05	34.2	171	0	0.58	4302	634	7.96	1.3	23.1	21	0.17	41	3.65	2.4	5.79	3.3
4-7-9-1-06	60.8	242	201	0.46	7039	782	207	4.45	13.6	13.7	0.6	49.9	3.66	1.78	7.35	3.39
4-7-9-1-07	36.7	215	84	0.74	6903	680	158	1.3	16	19.6	0.85	36	3.33	2.39	7.91	5.05
4-7-9-1-09	134	3287	849	0.55	7335	780	148	6.63	22.3	13.3	0.09	68.9	13.4	2.49	7.69	2.37
4-7-9-1-10	271	1924	472	1.42	6645	629	192	2.33	14.3	21.4	1.23	28.9	5	3.01	8.31	11.8
4-7-9-1-11	115	441	405	1.06	5246	972	206	2.61	12.5	21.3	0.05	74.7	4.07	2.03	6.84	4.61
LNT14-2-01	1102	5168	708	2.72	8767	1135	126	20.6	10	22.9	1.62	39.2	4.18	2.95	7.72	4.89
LNT14-2-02	782	3703	0	3.41	8897	1646	216	26.2	10.6	28.5	0.74	36.6	5.46	4.22	10.1	47.4
LNT14-2-03	1115	3774	43	2.59	6656	1499	236	30.1	11	24.7	12	47.5	5.14	2.07	6.73	36
LNT14-2-06	1508	4378	1254	15.37	7410	1679	6.51	27.5	10	28.7	3.37	22.1	3.96	2.81	6.16	2.74
Mean	496	1972	348	2.68	6593	945	126	13.2	15.9	22.2	1.86	46.6	4.81	2.55	7.42	13.7
S.D.	524	1879	395	4.06	1361	410	90.1	12.1	5.19	5	3.2	16.9	2.68	0.63	1.16	17.7
<i>Lannitang (Type II)</i>																
1-2-6-16	377	1775	11,745	1.56	2381	1335	197	7.77	28.7	45.7	36	11.2	1.67	3.72	4.17	7.28
1-2-7-04	632	1516	269	1.46	3922	2233	209	3.78	10	57.4	40.9	21.1	3.29	4.95	5.44	3.08
1-2-7-06	3532	4103	348	0.84	1244	1347	320	10.5	7.38	72.9	31.5	31.2	5.82	3.4	1.44	8.52
1-2-30-1-12	8062	700	46	1.25	3434	1363	68.5	6.82	7.9	10.9	2.76	66.4	4.19	2.99	2.26	21.9
Mean	3151	2024	3102	1.28	2745	1570	199	7.21	13.5	46.7	27.8	32.5	3.74	3.76	3.33	10.2
S.D.	3573	1460	5763	0.32	1190	443	103	2.76	10.2	26.4	17.1	24	1.73	0.84	1.82	8.14
<i>Disuga (Type I)</i>																
DSG11-18-04	295	1822	823	2.25	12,735	764	378	8.38	27.6	22	6.12	12.2	2.62	1.24	8.32	10.4
DSG11-18-05	28.1	49.1	255	1.9	13,179	690	346	4.76	25.3	21.3	2.38	12.4	1.96	0.55	9.12	0.36
DSG11-18-06	63.4	109	0	2.09	17,457	895	345	6.9	24.1	24.9	2.61	11.6	2.2	0.73	10.7	0.52
DSG11-18-07	15.3	54.1	33	1.15	17,465	1292	351	6.89	24.5	22.8	2.8	12.5	1.53	1.51	11.6	0.05
DSG11-18-08	13.4	48.9	0	1.53	17,184	980	351	5.54	23.8	22.8	2.36	12.3	2.1	0.59	11.3	0.21
DSG11-18-09	140	170	1591	1.32	16,842	1175	366	17.8	25.1	24.6	9.5	11.9	2.34	1.37	11.2	21.8
DSG11-18-10	33.3	164	47	1.76	9656	674	382	2.5	27.3	23.5	1.43	10.1	2.17	0.67	8.2	0.51
DSG11-22-02	665	1518	7363	10.8	18,088	993	701	1196	21	20.8	206	136.9	2.1	1.43	4.7	16.12
DSG11-22-05	404	1033	24,515	1.70	13,566	1496	599	350	17.9	17.3	3.03	30.6	2.65	1.46	4.52	5.07
DSG11-25-04	25.6	115	161	1.91	7594	1704	807	240	15.8	29.7	6.38	62.5	1.8	1.01	8.22	3.98
DSG11-25-09	1029	1114	1436	3.64	5622	841	654	188	17	26.9	36.9					

Table 2 (continued)

Samples	Mg	Al	Ca	Sc	Ti	V	Cr	Mn	Co	Ni	Cu	Zn	Ga	Ge	Sn	Pb
DSG11-22-01	454	611	53	0	541	1884	648	376	33.5	42.5	9.3	39	3.66	0.52	0.49	4.31
DSG11-25-02	20.5	83.5	868	0.86	1081	1192	625	212	18.4	44.6	23.4	185.2	1.35	1.01	1.09	7.58
DSG11-25-05	367	415	107	0.83	1603	1431	741	174	15	29.4	7.55	70.7	2.03	1.14	1.85	1.71
DSG11-25-07	161	244	1243	0.67	1061	1356	722	206	15.1	28.1	12.4	36.2	1.81	0.54	1.96	1.18
Mean	251	339	568	0.59	1072	1466	684	242	20.5	36.1	13.1	82.8	2.21	0.8	1.35	3.7
S.D.	197	227	584	0.4	433	296	56	91.2	8.8	8.61	7.1	70	1	0.32	0.69	2.93
<i>Tumugou Fm. andesite (Type I)</i>																
DSG10-3-03	187	1362	35,983	3.72	40,943	911	363	233	37.5	49.6	3	12.5	1.28	1.21	3.29	13
DSG10-3-04	83	732	31,260	2.35	40,522	734	965	258	42.4	60.7	4.02	15.4	1.57	1.07	3.08	22.2
DSG10-3-04	1286	1900	26,660	2.66	28,090	773	566	265	40.9	56.7	1.15	16.7	1.68	1.09	2.54	30.3
DSG10-3-06	121	425	4249	1.42	21,290	705	655	322	47.1	69.1	1.98	21.2	1.67	0.39	3.3	186
D07-3-2-05	228	1408	26,334	4.44	33,378	820	607	257	27.8	49	5.13	12.9	1.59	0.92	2.54	17.6
DSG11-31-02	76.4	108	1750	1.3	33,030	892	594	109	19.4	27.9	3.85	17.6	2.3	0.51	7.11	0.36
DSG11-31-03	158	755	2171	10.23	33,418	805	592	87.1	18.8	27.5	384	19.9	2.63	1.31	7.66	21.5
DSG11-31-04	13.2	36.8	53	1.56	27,363	637	601	51.9	20.2	25.9	2.61	12.9	2.24	0.66	6.4	0.19
DSG11-31-05	29.5	50.4	0	1.64	22,195	677	533	43.1	18.9	29.3	3.39	13.6	2.7	0.9	5.31	0.12
DSG11-31-06	60	75.4	126	1.82	28,663	713	559	62.1	21.1	25.4	1.83	12.7	2.18	0.65	6.82	0.2
DSG11-31-09	15.4	36.6	0	0.59	31,870	695	613	76.1	19.9	27.9	5.39	16.6	1.92	0.94	6.94	0.33
DSG11-31-10	350	623	12,378	1.8	23,399	707	549	45.7	20.2	30.2	237	16	2.38	0.89	6.07	3.44
Mean	217	626	11,747	2.79	30,347	756	600	151	27.9	39.9	54.4	15.7	2.01	0.88	5.09	24.6
S.D.	351	636	14,140	2.57	6449	86	136	106	10.9	16	124	2.89	0.46	0.28	1.98	52.1

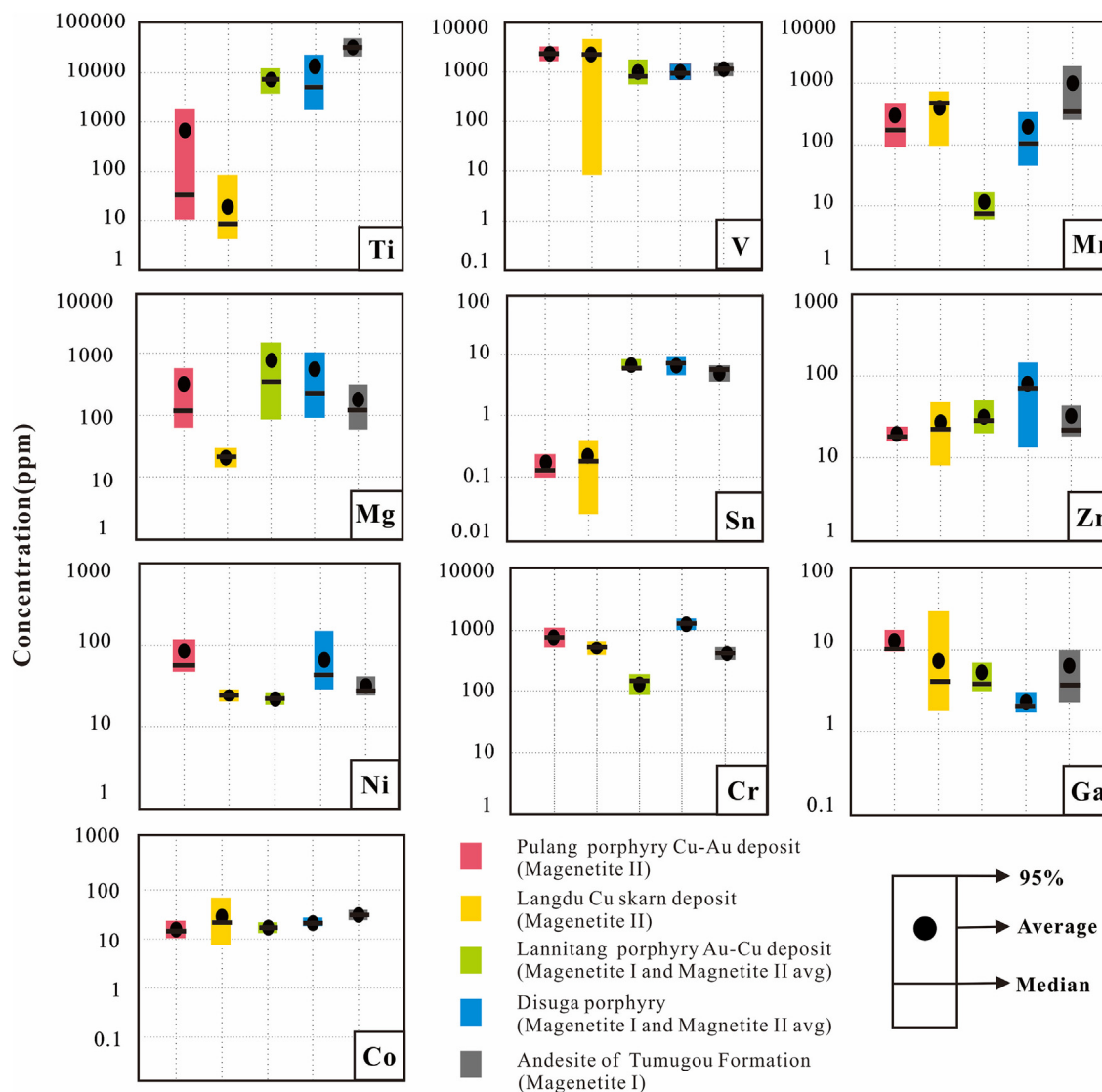


Fig. 10. Box plots for the magnetite compositions (ppm) in the Zhongdian region. The whiskers represent the upper and lower threshold values (95 percentile confidence interval). Median values are displayed as solid black lines and mean values as black dots.

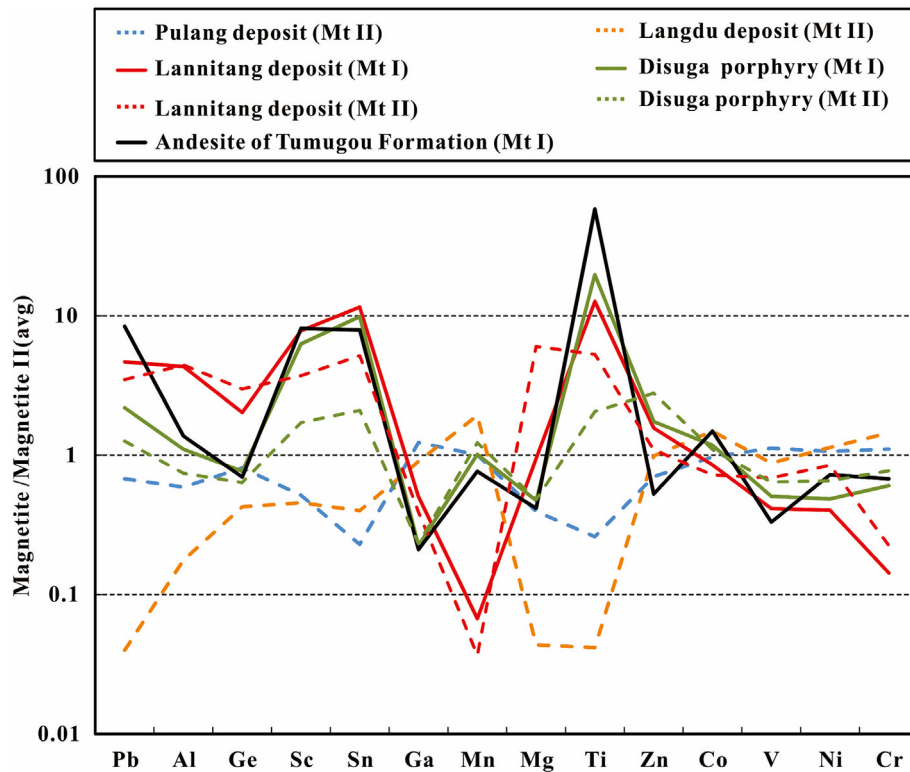


Fig. 11. Multi-element spider diagrams of magnetite samples from the Zhongdian region. Trace element concentrations in magnetite are normalized to the mean values of Magnetite II.

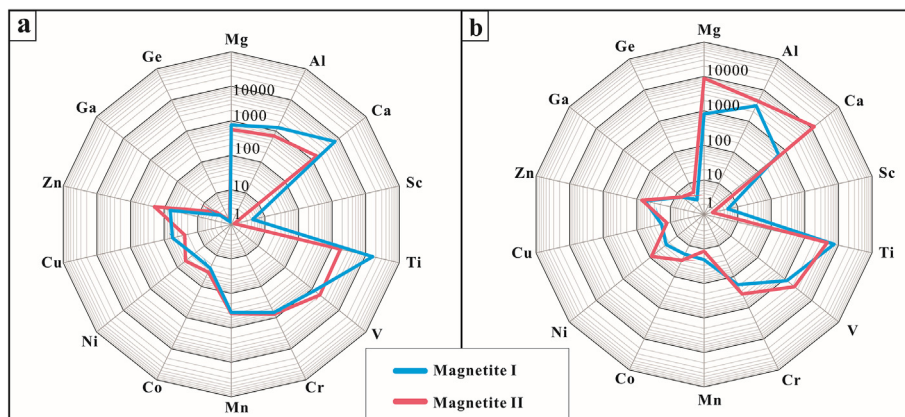


Fig. 12. Radar plots of Magnetite I and II from (a) porphyry at Disuga, and (b) Lannitang Au-Cu deposit.

agrees with many previous studies (Toplis and Corgne, 2002; Klemme et al., 2006; Righter et al., 2006).

6.3. Metallogenetic implications

In the last decades, many workers have attempted to chemically distinguish igneous magnetite (in the wall-rocks) from hydrothermal magnetite in porphyry-type deposits (Dare et al., 2014; Nadoll et al., 2015), and the discrimination diagrams of Ti vs. Ni/Cr (Dare et al., 2014) and Ti vs. V (Nadoll et al., 2015) were proposed. The behaviors of Cr and Ni are coupled in silicate magmas, with the Ni/Cr ratios typically < 1 , whereas they are decoupled (due to the higher solubility of Ni than Cr) in hydrothermal fluids, with Ni/Cr ratios ≥ 1 . However, our altered igneous Magnetite I and hydrothermal Magnetite II are both plotted in the “magmatic magnetite” field in the Ti vs. Ni/Cr diagram (Fig. 14b). The low Ni/Cr ratios could be caused by the relatively high average Cr contents in both Magnetite I (392 ppm) and Magnetite II,

(885 ppm). This relatively high Cr content is also observed in hydrothermal magnetites in porphyry deposits of southwestern United States and Ertsberg district (Nadoll et al., 2014, 2015), which yielded relatively low Ni/Cr ratios (< 1). Moreover, experimental studies showed that both Cr^{6+} and Cr^{3+} are more soluble than Ni in high (magmatic) temperature aqueous fluids (James, 2003; Watenphul et al., 2012, 2013), and that magmatic-hydrothermal magnetite may have low Ni/Cr ratios (< 1) (Huang et al., 2019). Our results are also consistent with previous studies, which suggested that the Ti vs. Ni/Cr plot (Dare et al., 2014) is not always useful to discriminate igneous from hydrothermal magnetites in porphyry systems (Knipping et al., 2015).

In the Ti vs. V diagram, igneous magnetite is characterized by higher Ti and V contents than hydrothermal magnetite (Nadoll et al., 2015). The high-Ti (average 16,646 ppm) Magnetite I cores fall mainly in the “magmatic magnetite” field outlined by Huang et al. (2019) (Fig. 14a). The low-Ti (average 520 ppm) Magnetite II grains fall mainly outside the “magmatic magnetite” and “hydrothermal

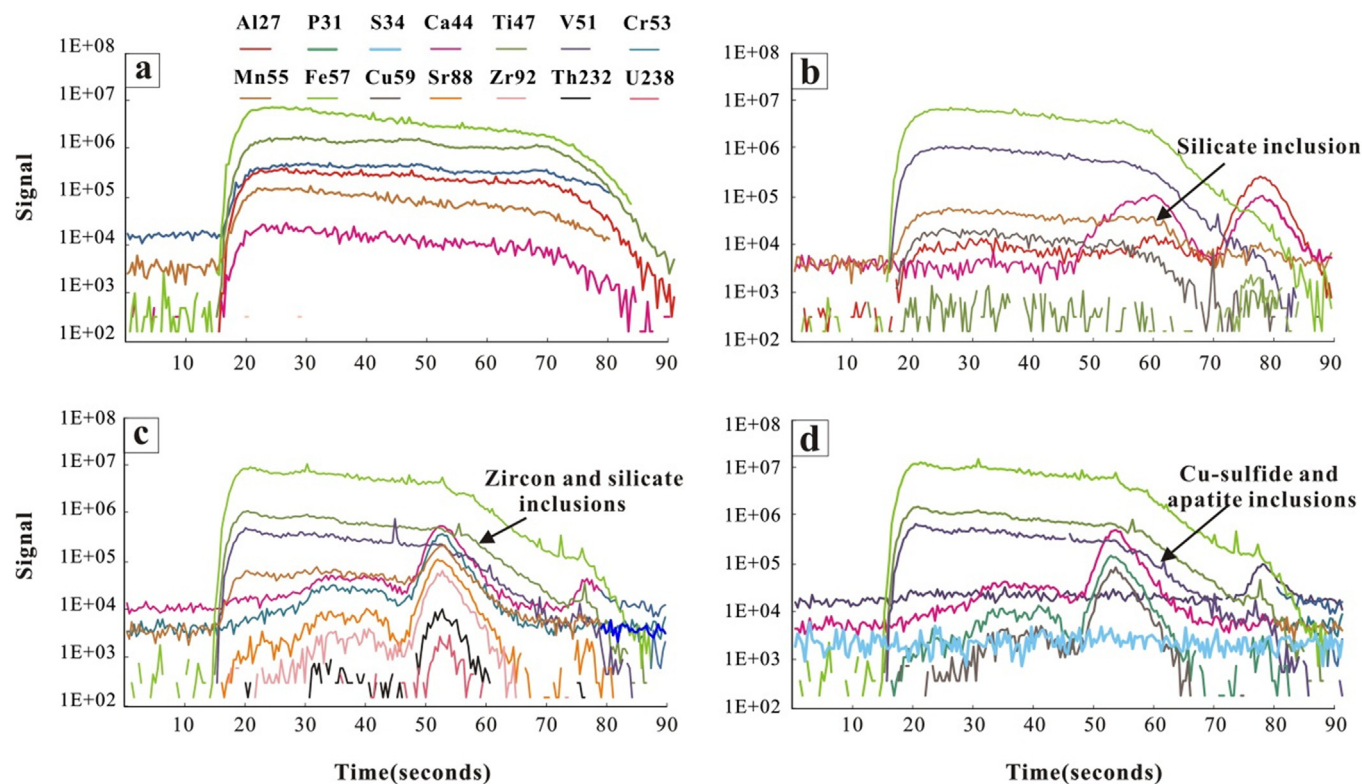


Fig. 13. LA-ICP-MS time-resolved signals of magnetite. (a) Flat spectral lines (e.g., Fe, Ti, V, Mn) indicate no mineral inclusions in magnetite (Magnetite I; Lannitang); (b) First half of stable signals indicate no inclusions, whereas the second half indicate the presence of silicate inclusion (Magnetite II; Pulang); (c) Zircon and apatite inclusions revealed by the occurrence of Th, U, Ca, Sr and Co spectral spikes (Magnetite I; andesite of Tumugou Formation); (d) Cu-sulfide inclusions revealed by the occurrence of Cu, S and Co spectral spikes (Magnetite I; Disuga porphyry).

magnetite” fields, and partly in the overlapping area of these two fields. This suggests that some Magnetite II grains may have a magmatic-hydrothermal origin (Knipping et al., 2015; Huang et al., 2019).

Many previous studies have linked the geochemistry of magnetite to the formation environments and genetic types of ore deposits (e.g., Lin, 1982; Dupuis and Beaudoin, 2011; Dare et al., 2014; Nadoll et al., 2014). A series of diagrams (e.g., (Ni + Cr) vs. (Si + Mg), (Al + Mn) vs. (Ti + V)) were proposed to discriminate different types of mineral deposits such as porphyry, skarn, banded iron formation (BIF), and Fe-Ti-V magmatic deposits. However, these diagrams may not be able to discriminate some ore deposits that have been intensely altered. For example, magnetite trace element compositions of the Chengchao skarn deposit (South China) are plotted in the “Skarn”, “IOCG” and “BIF” fields in the (Ca + Mn + Al) vs. (Ti + V) diagram (Hu et al., 2014), whilst magnetite grains from the much-altered oxide ores at the Kangdian IOCG deposit fall inside the “BIF” field in the same diagram (Chen et al., 2015). In this study, our magnetite samples were collected from different types of deposits and from different alteration zones. Some samples were also intensely hydrothermal altered. The fact that our data fall outside the conventional “porphyry field” also suggest that these diagrams cannot adequately discriminate porphyry-related deposits in the Zhongdian region (Fig. 15).

Previous studies have suggested that the magnetite in skarn deposits contains higher Al, Mn, Mg and Ca contents than the magnetite in porphyry deposits (Canil et al., 2016; Nadoll et al., 2014, 2015; Dare et al., 2014; Pisiak et al., 2014, 2017). Significant carbonate rock contamination for alteration fluid is a more plausible explanation for the enrichments of these elements (Einaudi, 1981; Meinert, 1987; Nadoll and Koenig, 2011). However, the magnetite from the Langdu Cu skarn deposit cannot be distinguished by high Al, Mn, Mg concentrations from the porphyry deposits at Pulang and Lannitang. This may be caused by that the studied magnetite samples were from the Langdu

porphyries, which lack features of interactions between fluid and carbonate rocks and lead to low (Al + Mn) contents (Fig. 15a). The much higher Cr concentration in our magnetite than typical hydrothermal magnetites in porphyry deposits have caused our data to plot outside the porphyry field (Fig. 15b). Therefore, we propose that the binary plots of Ti vs. Sc, V vs. Sn and Ga vs. Sn can better distinguish the different origins of magnetites in the Zhongdian region (Fig. 14f, h, i). Moreover, the Sn vs. Mn and V vs. Mn plots can distinguish the magnetite that formed under high $f\text{O}_2$ conditions (Fig. 16).

Despite economic mineralization is yet to be discovered in the porphyries at Disuga, our new results on magnetite suggest a good prospecting potential: 1) Magnetite II at Disuga shows similar compositions to those in the giant Pulang Cu-Au porphyry deposit (Figs. 14, 16); 2) Several Cu-sulfide inclusions, which are considered as a direct mineralization indicator, are also identified inside the Disuga magnetite. This conclusion is supported by the fact that the Disuga porphyry is intensely phyllitic- to propylitic-altered with minor quartz-sulfide veins/veinlets being found (Liu et al., 2014; author's unpublished data), probably indicating that the ore-related potassic alteration zone was still below the current exploration level.

7. Conclusions

Magnetite from various porphyry-related deposits in the Zhongdian region is found to contain similar textural and trace element characters. This includes the presence of ilmenite lamellae and micro-pores in Magnetite I and the texturally-homogeneous Magnetite II. Magnetite I has porous core and homogeneous rim. The core of Magnetite I is rich in Ti and Cr and contains ilmenite exsolution lamellae, indicative of a dominantly igneous origin. Magnetite I has numerous micro-pores in its core, sharp core-rim boundary, and irregular boundaries with its adjacent minerals. These petrographic features and the Ti-Fe variation in

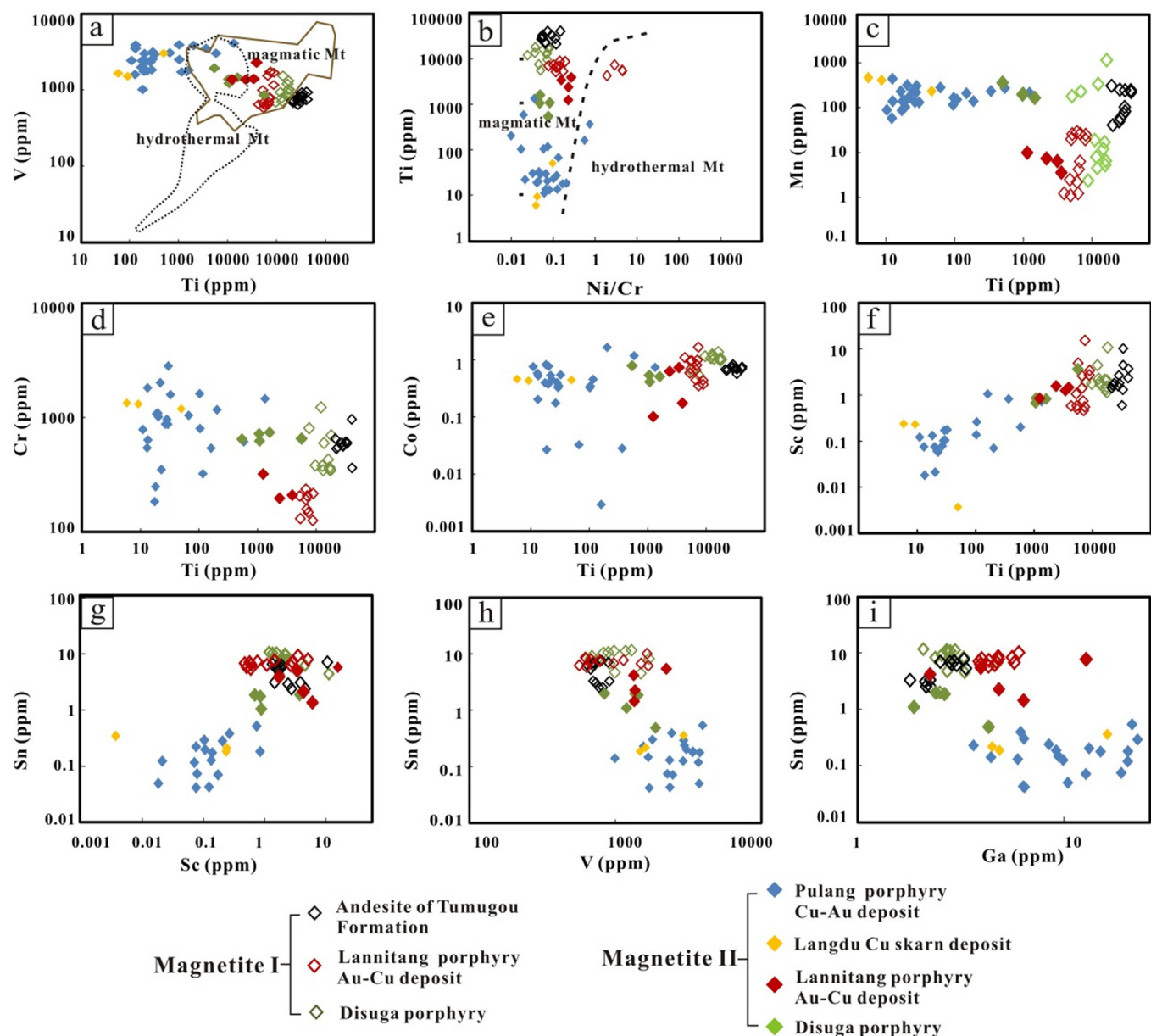


Fig. 14. Binary plots of (a) Ti vs. Ni/Cr, (b) V vs. Ti, (c) Cr vs. Ti, (d) Mn vs. Ti, (e) Co vs. Ti, (f) Sc vs. Ti, (g) Sn vs. Sc, (h) Sn vs. V, (i) Sn vs. Ga. LA-ICPMS data of the magnetite from the Tumugou Fm. andesite and porphyries at Pulang, Langdu, Lannitang and Disuga.

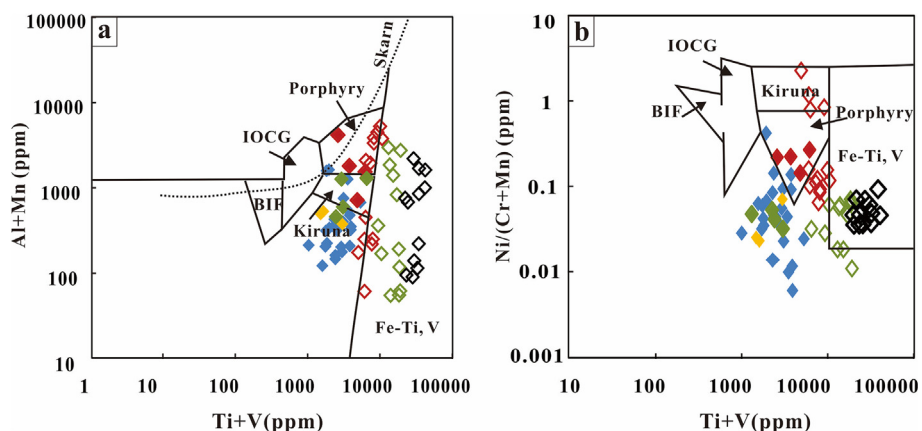


Fig. 15. Plots of (a) V + Ti vs. Al + Mn and (b) Ti + V vs. Ni/ (Cr + Mn) for the magnetite from the Tumugou Fm. andesite, porphyry at Disuga, and ore-bearing porphyries at Pulang, Langdu and Lannitang (redrawn from Nadoll et al., 2014). The legend in this figure is same as the legend in Fig. 14.

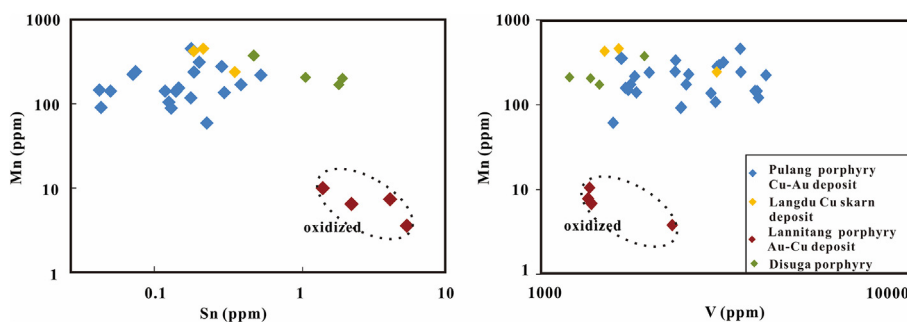


Fig. 16. Binary plots of (a) Sn vs. Mn and (b) V vs. Mn for the Magnetite II from the porphyries at Disuga, Pulang, Langdu, and Lannitang.

the core and rim indicate that Magnetite I may have undergone partial dissolution and reprecipitation.

Magnetite II grains have likely a hydrothermal origin. For the Zhongdian Cu-Au porphyry belt, we propose that the Sn vs. Mn and V vs. Mn plots can distinguish the magnetite formed under high f_{O_2} conditions. Moreover, the Ti vs. Sc, V vs. Sn and Ga vs. Sn plots may distinguish the different origins of magnetites.

LA-ICP-MS time-resolved signals suggest the presence of micro-/nano-scale inclusions of apatite, zircon, other silicates and minor sulfides in the magnetite. Magnetite II from the altered Disuga porphyries has similar texture and composition to its counterpart from the potassically-altered Pulang porphyries. Considering also the presence of Cu-sulfide inclusions in Disuga Magnetite I, we suggest significant mineralization potential in the Disuga porphyries.

Declaration of Competing Interest

The authors declare that they have no known competing financial interests or personal relationships that could have appeared to influence the work reported in this paper.

Acknowledgments

This work is supported by the National Key R&D Program of China (2018YFC0603505) and NSFC projects (41673051, 41373051). Wenqin Zheng, Xiang Li, Shaohua Dong, Yanwen Tang and Zhihui Dai are thanked for the laboratory assistance. We thank Franco Pirajno, Zhaochong Zhang and four anonymous reviewers for their constructive comments and suggestions.

Appendix A. Supplementary data

Supplementary data to this article can be found online at <https://doi.org/10.1016/j.oregeorev.2019.103245>.

References

- Angerer, T., Hagemann, S.G., Danyushevsky, L.V., 2012. Geochemical evolution of the banded iron formation-hosted high-grade iron ore system in the Koolyanobbing greenstone belt, Western Australia. *Econ. Geol.* 107, 599–644.
- Barnes, S.J., Roeder, P.L., 2001. The range of spinel composition in terrestrial mafic and ultramafic rocks. *J. Petrol.* 42, 2279–2302.
- Boulvais, P., Ruffet, G., Cornicet, J., Mermet, M., 2007. Cretaceous albitization and dequartzification of Hercynian peraluminous granite in the Salvezines Massif (French Pyrénées). *Lithos* 93 (1–2), 89–106.
- Buddington, A.F., Lindsley, D.H., 1964. Iron-titanium oxide minerals and synthetic equivalents. *J. Petrol.* 5, 310–357.
- Canil, D., Grondahl, C., Lacourse, T., Pisiak, L.K., 2016. Trace elements in magnetite from porphyry Cu-Mo-Au deposits in British Columbia. *Canada. Ore Geol. Rev.* 72, 1116–1128.
- Chen, H.Y., Han, J.S., 2015. Study of magnetite: Problem and future. *Bull. Miner. Petro. Geochem.* 34 (4), 724–730 (in Chinese with English abstract).
- Chen, W.T., Zhou, M.F., Li, X.C., Gao, J.F., Hou, K.J., 2015. In-situ LA-ICP-MS trace elemental analyses of magnetite: Cu-(Au, Fe) deposits in the Khetri copper belt in Rajasthan Province. NW India. *Ore Geol. Rev.* 65, 929–939.
- Chung, D., Zhou, M.F., Gao, J.F., Chen, W.T., 2015. In-situ LA-ICP-MS trace elemental analyses of magnetite: the late Paleoproterozoic Sokoman Iron Formation in the Labrador Trough, Canada. *Ore Geol. Rev.* 65, 917–928.
- Cornell, R.M., Schwertmann, U., 2003. The Iron Oxides: Structure, Properties, Reactions, Occurrences, and Uses, second ed. Weinheim, Wiley-VCH.
- Dare, S.A.S., Barnes, S.J., Beaudoin, G., 2012. Variation in trace element content of magnetite crystallized from a fractionating sulfide liquid, Sudbury, Canada: implications for provenance discrimination. *Geochim. Cosmochim. Acta* 88 (7), 27–50.
- Dare, S.A.S., Barnes, S.J., Beaudoin, G., Méric, J., Boutroy, E., Potvin, D.C., 2014. Trace elements in magnetite as petrogenetic indicators. *Miner. Depos.* 49 (7), 785–796.
- Duan, C., Li, Y.H., Yuan, S.D., Hu, M.Y., Zhao, L.H., Chen, X.D., Zhang, C., Liu, J.L., 2012. Geochemical characteristics of magnetite from Washan iron deposit in Ningwu ore district and its constraints on ore-forming. *Acta Petrol. Sin.* 28 (1), 243–257 (in Chinese with English abstract).
- Duan, S.G., Dong, M.H., Zhang, Z.H., Jiang, Z.S., Li, F.M., 2014. A LA-ICP-MS analysis of elements in magnetite from Dunde iron deposit in Western Mountains, Xinjiang constrains on genesis of the deposit. *Miner. Depos.* 33 (6), 1325–1337 (in Chinese with English abstract).
- Dupuis, C., Beaudoin, G., 2011. Discriminant diagrams for iron oxide trace element fingerprinting of mineral deposit types. *Miner. Depos.* 46 (4), 319–335.
- Einaudi, M.T., 1981. Description of skarns associated with porphyry copper plutons. In: Titley, S.R. (Ed.), *Advances in Geology of the Porphyry Copper Deposits*. The University of Arizona Press, Tucson, pp. 139–183.
- Frost, B.R., Lindsley, D.H., 1991. Occurrence of iron-titanium oxides in igneous rocks. In: Lindsley D.H. (Eds.), *Oxide Minerals: Petrologic and Magnetic Significance*. Rev. Mineral., Mineral. Soc. Am. pp. 433–462.
- Geisler, T., Schaltegger, U., Tomaschek, F., 2007. Re-equilibration of zircon in aqueous fluids and melts. *Elements*, 3, 43–50.
- Ghiorso, M.S., Sack, O., 1991. Thermochemistry of the oxide minerals. In: Lindsley, D.H. (Eds.), *Oxide Minerals: Petrologic and Magnetic Significance*. Mineral. Soc. Am. pp. 221–264.
- Gustafson, L.B., Hunt, J.P., 1975. The porphyry copper deposit at El Salvador, Chile. *Econ. Geol.* 70, 857–912.
- Hemley, J.J., Hunt, J.P., 1992. Hydrothermal ore-forming processes in the light of studies in rock-buffered systems; II, Some general geologic applications. *Econ. Geol.* 87, 23–43.
- Hu, H., Duan, Z., Yan, L., Li, J.W., 2014a. Trace element systematics of magnetite from the Chengchao iron deposit in the Daye district: A laser ablation ICP-MS study and insight into ore genesis. *Acta Petrol. Sin.* 30 (5), 1292–1306 (in Chinese with English abstract).
- Hu, H., Li, J.W., Lentz, D., Ren, Z., Zhao, X.F., Deng, X.D., Hall, D., 2014b. Dissolution-reprecipitation process of magnetite from the Chengchao iron deposit: insights into ore genesis and implication for in-situ chemical analysis of magnetite. *Ore Geol. Rev.* 57, 393–405.
- Hu, H., Lentz, D., Li, J.W., McCarron, T., Zhao, X.F., Deng, X.D., Hall, D., 2015. Re-equilibration processes in magnetite from iron skarn deposits. *Econ. Geol.* 110, 1–8.
- Huang, X.W., Zhao, X.F., Qi, L., Zhou, M.F., 2013. Re-Os and S isotopic constraints on the origins of two mineralization events at the Tangdan sedimentary rock-hosted stratiform Cu-deposit, SW China. *Chem. Geol.* 347, 9–19.
- Huang, X.W., Sappin, A.A., Boutroy, E., Beaudoin, G., Makvandi, S., 2019. Trace element composition of igneous and hydrothermal magnetite from porphyry deposits: relationship to deposit subtypes and magmatic affinity. *Econ. Geol.* 114 (5), 917–952.
- Hou, Z.Q., Yang, Y.Q., Wang, H.P., Qu, X.M., Lv, Q.T., Huang, D.H., Wu, X.Z., Yu, J.J., Tang, S.H., Zhao, J.H., 2003. Collision-orogenic Progress and Mineralization System of Yidun Arc. Geological Publishing House, Beijing, pp. 345 (in Chinese).
- James, B.R., 2003. Chromium. In: Stewart, B.A., Howell, T.A. (Eds.), *Encyclopedia of Water Science*. New York: Marcel Dekker, pp. 77–82.
- Kaur, P., Chaudhri, N., Hofmann, A.W., Raczk, I., Okrusch, M., Baumgartner, S.S., 2012. Two-stage, extreme albitization of A-type granites from Rajasthan, NW India. *J. Petrol.* 53 (5), 919–1548.
- Knipping, J.L., Bilenker, L.D., Simon, A.C., Reich, M., Barra, F., Deditius, A.P., Wölle, M., Heinrich, C.A., Holtz, F., Munizaga, R., 2015. Trace elements in magnetite from massive iron oxide-apatite deposits indicate a combined formation by igneous and magmatic-hydrothermal processes. *Geochim. Cosmochim. Acta* 171, 15–38.
- Klemme, S., Günther, D., Hametner, K., Prowatke, S., Zack, T., 2006. The partitioning of trace elements between ilmenite, ulvöspinel, armalcolite and silicate melts with implications for the early differentiation of the moon. *Chem. Geol.* 234, 251–263.
- Leng, C.B., Zhang, X.C., Hu, R.Z., Wang, S.X., Zhong, H., Wang, W.Q., Bi, X.W., 2012. Zircon U-Pb and molybdenite Re-Os geochronology and Sr-Nd-Pb-Hf isotopic

- constraints on the genesis of the Xuejiping porphyry copper deposit in Zhongdian, Northwest Yunnan, China. *J. Asian Earth Sci.* 60, 31–48.
- Leng, C.B., Huang, Q.Y., Zhang, X.C., Wang, S.X., Zhong, H., Hu, R.Z., Bi, X.W., Zhu, J.J., Wang, X.S., 2014. Petrogenesis of the Late Triassic volcanic rocks in the Southern Yidun arc, SW China: Constraints from the geochronology, geochemistry, and Sr-Nd-Pb-Hf isotopes. *Lithos* 190–191 (2), 363–382.
- Leng, C.B., Gao, J.F., Chen, T.W., Zhang, X.C., Tian, Z.D., 2018. Platinum-group elements, zircon Hf-O isotopes, and mineralogical constraints on magmatic evolution of the Pulang porphyry Cu-Au system, SW China. *Gondwana Res.* 62, 163–177.
- Li, G.M., Li, J.X., Qin, K.Z., Zhang, T.P., Xiao, B., 2007. High temperature, salinity and strong oxidation ore-forming fluid at Duobuba gold-rich porphyry copper deposit in the Bangonghu tectonic belt, Evidence from fluid inclusions. *Acta Petrol. Sin.* 23 (5), 935–952 (in Chinese with English abstract).
- Li, J.X., Qin, K.Z., Li, G.M., 2006. Basic characteristics of gold-rich porphyry copper deposits and their ore sources and evolving process of high oxidation magma and ore-forming fluid. *Acta Petrol. Sin.* 22 (3), 678–688 (in Chinese with English abstract).
- Li, W.C., Zeng, P.S., Hou, Z.Q., White, N.C., 2011. The Pulang porphyry copper deposit and associated felsic intrusions in Yunnan Province, southwest China. *Econ. Geol.* 106, 79–92.
- Li, W., Yang, Z., Cao, K., Lu, Y., Sun, M., 2019. Redox-controlled generation of the giant porphyry Cu-Au deposit at Pulang, southwest China. *Contrib. Mineral. Petro.* 174.
- Li, Y.R., Fan, Y.H., Meng, Q., 2009. The Langdu skarn Cu deposit in northwest Yunnan. *Yunnan Geol.* 28 (2), 137–142 (in Chinese with English abstract).
- Lin, S.Z., 1982. Study on the chemical genesis and evolution of magnetite. *Acta Miner. Sin.* 3, 166–174 (in Chinese with English abstract).
- Lindsley, D.H., 1976. The crystal chemistry and structure of oxide minerals as exemplified by the Fe-Ti oxides. In: Rumble III, D. (Eds.), *Oxide Minerals*. Mineral Soc. Am. pp. 1–60.
- Liu, J., Yang, L., Lu, L., 2013. Pulang reduced porphyry copper deposit in the Zhongdian area, Southwest China: Constraints by the mineral assemblages and the ore-forming fluid compositions. *Acta Petrol. Sin.* 29, 3914–3924.
- Liu, P.P., Zhou, M.F., Chen, W.T., Gao, J.F., Huang, X.W., 2015. In-situ LA-ICP-MS trace elemental analyses of magnetite: Fe-Ti-(V) oxide-bearing mafic-ultramafic layered intrusions of the Emeishan Large Igneous Province, SW China. *Ore Geol. Rev.* 65, 853–871.
- Liu, X.L., Li, W.C., Zhang, N., Yin, G.H., Deng, M.G., 2014. Geochronological, geochemical characteristics of Disuga ore-forming I-type granitic porphyries in the Geza arc, Yunnan Province and their geological significance. *Geol. Rev.* 60 (1), 103–114 (in Chinese with English abstract).
- Liu, Y.S., Hu, Z.C., Gao, S., Gunther, D., Chang, J.X., Gao, C.G., Chen, H.H., 2008. In-situ analysis of major and trace elements of anhydrous minerals by LA-ICP-MS without applying an internal standard. *Chem. Geol.* 257, 34–43.
- Lowell, J.D., Gilbert, J.M., 1970. Lateral and vertical alteration-mineralization zoning in porphyry ore deposits. *Econ. Geol.* 65, 373–408.
- Meinert, L.D., 1987. Skarn zonation and fluid evolution in the Groundhog Mine, Central mining district, New Mexico. *Econ. Geol.* 82 (3), 523–545.
- Meinert, L.D., Dipple, G.M., Nicolsescu, S., 2005. World skarn deposits. *Economic Geology 100th Anniversary Volume*. 299–336.
- McQueen, K.G., Cross, A.J., 1998. Magnetite as a geochemical sampling medium: application to skarn deposits. In: Eggleton, R.A. (Ed.), *The State of the Regolith*. Geological Society of Australia, Brisbane, pp. 194–199.
- Nadoll, P., Koenig, A.E., 2011. LA-ICP-MS of magnetite: methods and reference materials. *J. Anal. Atom. Spectro.* 26 (9), 1872–1877.
- Nadoll, P., Mauk, J.L., Hayes, T.S., Koenig, A.E., Box, S.E., 2012. Geochemistry of magnetite from hydrothermal ore deposits and host rocks of the mesoproterozoic belt supergroup, United States. *Econ. Geol.* 107 (60), 1275–1292.
- Nadoll, P., Angerer, T., Mauk, J.L., French, D., Walshe, J., 2014. The chemistry of hydrothermal magnetite: a review. *Ore Geol. Rev.* 61 (5), 1–32.
- Nadoll, P., Mauk, J.L., Leveille, R.A., Koenig, A.E., 2015. Geochemistry of magnetite from porphyry Cu and skarn deposits in the southwestern United States. *Miner. Depos.* 50, 493–515.
- Oyarzún, R., Mírquez, A., Lillo, J., 2001. Giant versus small copper deposits of Cenozoic age in northern Chile: adakite versus normal calc-alkaline magmatism. *Miner. Depos.* 36, 794–798.
- Pang, Z.S., Du, Y.S., Wang, G.W., Guo, X., Cao, Y., Li, Q., 2009. Single-grain zircon U-Pb isotopic ages, geochemistry and its implication of the Pulang complex in Yunnan Province, China. *Acta Petrol. Sin.* 25, 159–165 (in Chinese with English abstract).
- Pecoits, E., Gingras, M.K., Barley, M.E., Kappler, A., Posth, N.R., Konhauser, K.O., 2009. Petrography and geochemistry of the Dales Gorge banded iron formation: Paragenetic sequence, source and implications for paleo-ocean chemistry. *Precambrian Res.* 172, 163–187.
- Pisiak, L.K., Canil, D., Grondahl, A., Plouffe, T., Ferbey, R.G., 2014. Magnetite as a porphyry Cu indicator mineral in till: a test using the Mount Polley porphyry Cu-Au deposit, British Columbia. *B.C. Report 2015-1. Geo. Sci.* 141–149.
- Pisiak, L.K., Canil, D., Lacourse, T., Plouffe, A., Ferbey, T., 2017. Magnetite as an indicator mineral in the exploration of porphyry deposits: a case study in till near the Mount Polley Cu-Au deposit, British Columbia, Canada. *Econ. Geol.* 112, 919–940.
- Putnis, C.V., 2005. Direct observations of pseudomorphism: compositional and textural evolution at a fluid-solid interface. *Am. Mineral.* 90, 1909–1912.
- Putnis, C.V., 2009. Mineral replacement reactions. *Rev. Mineral. Geochem.* 70, 87–124.
- Rabbia, O.M., Laura, B.H., David, H.F., Robert, W.K., John, C., 2009. The El Teniente porphyry Cu-Mo deposit from hydrothermal rutile perspective. *Miner. Depos.* 1–18.
- Rabbia, O.M., 2012. Crystal chemistry of rutile and anatase in Andean porphyry deposits, evaluation of its use as monitor of metal activity in crustal hydrothermal fluids. Universidad de Chile. 147.
- Ren, T., Zhong, H., Zhang, X.C., Han, R.S., Ma, M.J., 2013. Mineralogical characteristics of skarns in Langdu skarn copper deposit, Zhongdian, Yunnan Province, China. *Acta Miner. Sin.* 33 (3), 278–286 (in Chinese with English abstract).
- Righter, K., Sutton, S.R., Newville, M., Le, L., Schwandt, C.S., Uchida, H., Lavina, B., Downs, R.T., 2006. An experimental study of the oxidation state of vanadium in spinel and basaltic melt with implications for the origin of planetary basalt. *Am. Mineral.* 91, 1643–1656.
- Rui, Y., Huang, Z.K., Qi, G.M., Xu, Y., Zhang, H.T., 1984. The porphyry Cu (Mo) deposit in China. Beijing: Geological Publishing House, pp. 119–122 (in Chinese with English abstract).
- Sidhu, P.S., Gilkes, R.J., Posner, A.M., 1981. Oxidation and ejection of nickel and zinc from natural and synthetic magnetites. *Soil sci. Soc. Am. J.* 45, 641–644.
- Sillitoe, R.H., 2010. Porphyry copper systems. *Econ. Geol.* 105 (105), 3–41.
- Sun, W.D., Liang, H.Y., Ling, M.X., Zhan, M.Z., Ding, X., Zhang, H.X., Yang, Y., Li, Y.L., Ireland, T.R., Wei, Q.R., 2013. The link between reduced porphyry copper deposits and oxidized magmas. *Geochim. Cosmochim. Acta* 103 (2), 263–275.
- Toplis, M.J., Corgne, A., 2002. An experimental study of element partitioning between magnetite, clinopyroxene and iron-bearing silicate liquids with emphasis on vanadium. *Contrib. Mineral. Petro.* 144, 22–37.
- Wang, B.Q., Zhou, M.F., Li, J.W., Yan, D.P., 2011. Late Triassic porphyritic intrusions and associated volcanic rocks from the Shangri-La region, Yidun terrane, Eastern Tibetan Plateau: Adakitic magmatism and porphyry copper mineralization. *Lithos* 127, 24–38.
- Wang, B.Q., Zhou, M.F., Chen, W.T., Gao, J.F., Yan, D.P., 2013a. Petrogenesis and tectonic implications of the Triassic volcanic rocks in the northern Yidun Terrane, Eastern Tibet. *Lithos* 175–176, 285–301.
- Wang, B.Q., Wang, W., Chen, W.T., Gao, J.F., Zhao, X.F., Yan, D.P., Zhou, M.F., 2013b. Constraints of detrital zircon U-Pb ages and Hf isotopes on the provenance of the Triassic Yidun Group and tectonic evolution of the Yidun Terrane, Eastern Tibet. *Sediment. Geol.* 289, 74–98.
- Wang, M.F., Wang, W., Liu, K., Michalak, P.P., Wei, K.T., Hu, M.Y., 2017. In-situ LA-ICP-MS trace elemental analyzes of magnetite: the Tieshan skarn Fe-Cu deposit, Eastern China. *Chem. Erde-Geochem.* 77 (1), 169–181.
- Wang, R.C., Yu, A.P., Chen, J., Xie, L., Lu, J.J., Zhu, J.C., 2012. Cassiterite exsolution with ilmenite lamellae in magnetite from the Huashan metaluminous tin granite in southern China. *Mineral. Petro.* 105, 71–84.
- Wang, S.X., Zhang, X.C., Leng, C.B., Qin, C.J., Ma, D.Y., Wang, W.Q., 2008. Zircon SHRIMP U-Pb dating of Pulang porphyry copper deposit, northwestern Yunnan, China: the ore-forming time limitation and geological significance. *Acta Petrol. Sin.* 24 (10), 2313–2321 (in Chinese with English abstract).
- Watenphul, A., Schmidt, C., Scholten, L., 2012. First insights into Cr³⁺ solubility in aqueous fluids at elevated P and T by m-XRF: 1st European Mineralogical Conference (EMC): Frankfurt, Germany, Abstract 544.
- Watenphul, A., Scholten, L., Kavner, A., Alraun, P., Falkenberg, G., Newville, M., Lanzirotti, A., Schmidt, C., 2013. Cu and Ni solubility in high-temperature aqueous fluids: American Geophysical Union (AGU), Fall Meeting, San Francisco, California, Abstract MR33A-2311.
- Wen, G., Li, J.W., Hofstra, A.H., Koenig, A.E., Lowers, H.A., Adams, D., 2017. Hydrothermal reequilibration of igneous magnetite in altered granitic plutons and its implications for magnetite classification schemes: Insights from the Handan-Xingtai iron district, North China Craton. *Geochim. Cosmochim. Acta* 215 (15), 255–270.
- Wechsler, B.A., Lindsley, D.H., Prewitt, C.T., 1984. Crystal structure and cation distribution in titanomagnetites ($(Fe_{2-x}Ti_xO_4)$). *Am. Mineral.* 69, 754–770.
- White, A.F., Peterson, M.L., Hochella, M.F., 1994. Electrochemistry and dissolution kinetics of magnetite and ilmenite. *Geochim. Cosmochim. Acta* 58, 1859–1875.
- Wu, C., Chen, H.Y., Hong, W., Li, D.F., Liang, P., Fang, J., Zhang, L.J., Lai, C.K., 2019. Magnetite chemistry and implications for the magmatic-hydrothermal ore-forming process: An example from the Devonian Yuleken porphyry Cu system, NW China. *Chem. Geol.* 522, 1–15.
- Xie, Q.H., Zhang, Z.C., Hou, T., Jin, Z.L., Santosh, M., 2017. Geochemistry and oxygen isotope composition of magnetite from the Zhangmatun deposit, North China Craton: Implications for the magmatic-hydrothermal evolution of Cornwall-type iron mineralization. *Ore Geol. Rev.* 88, 57–70.
- Yang, N.Q., 1982. A study of Sn⁴⁺ in the lattice of magnetite. *J. Miner. Petrol.* 1, 15–28.
- Yu, Y.F., Fei, G.C., Li, Y.G., Long, X.R., Tian, E.Y., Liu, G.Q., Lv, F.M., Hua, K.Q., 2016. Oxygen fugacity of intrusions from Lannitang porphyry copper deposit in Zhongdian Island arc, Yunnan: Implications for mineralization. *J. Miner. Petrol.* 143, 28–36 (in Chinese with English abstract).
- Yunnan Bureau of Geology and Mineral Resources (YBGR), 1999. Yunnan Geological Map series in scale of 1: 50000: Qiansui Sheet (H47E023016) and Hongshan Sheet (H47E024016) (in Chinese).
- Zeng, P.S., Mo, X.X., Yu, X.H., Hou, Z.Q., Xu, Q.D., Wang, H.P., Li, H., Yang, C.Z., 2003. Porphyry deposits and porphyry copper of Zhongdian area in northwest Yunnan. *Miner. Depos.* 22, 325–333 (in Chinese with English abstract).
- Zeng, P.S., Li, W.C., Wang, H.P., Li, H., 2006. The Indosian Pulang superlarge porphyry copper deposit in Yunnan, China: Petrology and chronology. *Acta Petrol. Sin.* 22 (4), 989–1000 (in Chinese with English abstract).
- Zhao, W.W., Zhou, M.F., 2015. In-situ LA-ICP-MS trace elemental analyses of magnetite: the Mesozoic Tengtung skarn Fe deposit in the Nanling Range, South China. *Ore Geol. Rev.* 65, 872–883.